Image-clustering analysis of the wave-structure interaction processes under breaking and non-breaking waves

Published Version:
Formentin S.M., Gaeta M.G., De Vecchis R., Guerrero M., Zanuttigh B. (2021). Image-clustering analysis of the wave-structure interaction processes under breaking and non-breaking waves. PHYSICS OF FLUIDS, 33(10), 1-18 [10.1063/5.0065019].

Availability:
This version is available at: https://hdl.handle.net/11585/853503 since: 2022-02-06

Published:
DOI: http://doi.org/10.1063/5.0065019

(Article begins on next page)

Manuscript submitted to Physics of Fluids for review and possible publication

IMAGE-CLUSTERING ANALYSIS OF THE WAVE-STRUCTURE INTERACTION PROCESSES UNDER BREAKING AND NON-BREAKING WAVES

Sara Mizar Formentin[1], Maria Gabriella Gaeta[1], Roberto De Vecchis[1], Massimo Guerrero[1] and Barbara Zanuttigh[1].

[(1)] Department of Civil, Chemical, Environmental and Materials Engineering, University of Bologna, Viale del Risorgimento 2, Bologna 40136, Italy.
saramizar.formentin2@unibo.it

Abstract

This contribution presents the effectiveness and the potentialities of a consolidated technique – the video-cluster analysis – to the study of turbulent flow and breaking waves, in order to demonstrate its suitability as a low-cost, non-intrusive method to derive quantitative key parameters describing the wave-structure interaction processes at coastal defense structures. To this purpose, a new methodology, consisting of a series of pre- and post-processing techniques developed to optimize the automatic detection of clusters in video imagery, was designed to process the video-records of experiments of wave run-up and wave overtopping at sea-dikes subjected to irregular waves. The results of the cluster analysis were elaborated to reconstruct the instantaneous profiles of the free-surface elevations across the structure crest and derive simultaneous information on overtopping volumes, discharges, depths and velocities, and to get spatial-time maps of the concentration of the air entrapped in the liquid phase. The accuracy of the methodology is demonstrated by comparing the quantities derived from the cluster analysis to laboratory measurements performed with resistive gauges and acoustic Doppler profilers. The novelty of the work is either represented by the results of the application of the cluster-analysis and by the procedures of optimizations, whose ensemble may establish a best practice and represent a guideline for other applications.

Keywords: Videography; cluster analysis; wave-structure interaction; wave overtopping; air entrainment; crown walls

1. Introduction

The analysis of the interaction processes between waves and coastal structures is still a challenging task, due to the highly turbulent flow conditions, the non-linear dynamics, the occurrence of the wave breaking and the air entrainment (Aleixo et al., 2018; Raby et al., 2020; Stringari et al., 2021). Time and spatial resolution of the measurement techniques poses limitations to the type and accuracy of the observations such as the size and distribution of the bubbles in the water flow (Na et al., 2015).

Different traditional measurements or combinations of measurements are available, including impedance probes (Waniewski et al., 2001; Cox and Shin, 2003), conductivity probes (Chanson, 2002; Hoque and Aoki, 2005; Mori et al., 2007), optical fibre probes (Blenkinsopp and Chaplin, 2007; Lim et al., 2008), imaging and acoustics-based methods (Deane and Stokes, 2002; Gaeta et al. 2020), imaging and optical fibre techniques (Rojas and Loewen, 2010; Na et al., 2015), dual-tip resistance-type probe and Acoustic Doppler Velocimeters (Mori and Kakuno, 2008). Since the 2010's, the widespread use of laser scanners prompted a number of successful applications related to the monitoring of the wave motion (Blenkinsopp et al. 2012; Streicher et al., 2013) and to the wave run-up and overtopping at coastal dikes (Hofland et al., 2015).

The development of Particle Image Velocimetry (PIV) in the 2000s provided a powerful technology to analyze velocity and turbulence fields in breaking waves (a.o. Oh et al. 2008; Drazen and Melville, 2009), with some limitations due to the unsteady, non-linear, high-speed process. Techet and McDonald (2005) concluded that significant improvements to the air seeding technique were needed to increase the flow resolution and resolve small scale vorticity. Kimmoun and Branger (2007) observed that the main difficulties in the PIV application were to automatically detect the free surface during wave breaking and to avoid laser light reflection by the air bubbles toward the camera. Duz et al. (2020) analysed the kinematics of spilling and plunging breakers, highlighting that the main measurement challenges are the reflections from the air/water interface and from the air entrapped in the breaking region, while the main post-processing challenges were due to the huge number of images and to the application of masking algorithm. Recent works highlighted that the PIV measurements are still extremely "expensive" (i.e. time consuming). Lim et al. (2015) measured the flow properties in the aerated crest of a plunging breaker by using modified PIV and bubble image velocimetry (BIV). The authors spent several months to complete the 20 repeated runs of the same tested condition to collect data from all the available measurement devices, finding that the generated waves were highly repeatable only before breaking.

Another peculiar technique to detect the wave breaking is represented by the use of infrared imagery, based on the fact that the surface temperature of the ocean is generally a few tenths of degrees Celsius less than the bulk water temperature immediately below (Robinson et al., 1984). Breaking waves momentarily disrupt the cool skin layer and the surface temperature becomes approximately equal to the bulk water temperature. The effectiveness of the infrared imagery to the detection of the wave breaking has been investigated for deep water (Jessup et al., 1997a), microbreaking waves (Jessup et al., 1997b) and, more recently, in the surf zone

(Carini et al., 2015). Siddiqui et al. (2001) employed simultaneously the infrared imagery and the measurements analysis to reconstruct the velocity fields of breaking waves, while Buscombe and Carini (2019) applied deep convolutional neural networks to classify the wave breaking type (e.g., non-breaking, spilling, plunging) from infrared imagery of the surf zone.

Summarizing, the direct measurement of the wave breaking characteristics requires the introduction of numerous instruments during the same campaign, such as resistant gauges, velocimeters, water volume trapping in tanks, pressure sensors, PIV – which may be unaffordable for economic and practical reasons. Furthermore, especially at small scales of laboratory tests, such a huge installation of instrumentation might not be recommendable due to the potential disturbance to the investigated processes (Soares-Frazão et al., 2009).

A relatively economic and non-intrusive alternative to the traditional techniques is represented by the use of video imagery, whose application in the coastal engineering is long-term lasting. For several decades, the coastal image data collected by monitoring systems such as ARGUS (Holman and Stanley, 2007) were elaborated to detect the wave characteristics (De Vries et al., 2011; Bechle and Wu, 2011), and to measure the wave run-up (Almar et al., 2017) on beaches. The diffusion of high-resolution digital camera allowed relatively simpler and cheaper applications of the videography, from the detection of the wave breaking on beaches (Almar et al., 2012) to the analysis of the wave viewing angle (Perugini et al., 2019). Vousdoukas et al. (2014) combined the laser scanning technique to a video camera monitoring to model the free-surface elevation and the wave-by-wave morphological changes in the swash and surf zones. Advances on the stereo processing of sea surface waves (Benetazzo et al., 2015) highly reduced the computational resources required to analyze a sequence of stereo images, allowing the employment of fast stereo video imaging and 2D laser slope gauge study in laboratory to gain information on the three-dimensional structure of the wind-wave field (Zavadsky et al., 2017). Gaeta et al. (2020) combined monostatic ultrasound velocity profiler to low cost videography which eventually provided the overtopping discharge at scaled dikes in laboratory. The results of these hybrid technologies highlighted that the use of the video camera may add valuable information to the laser scanner and improve the accuracy of the results.

Imagery-based analyses often require a significant amount of calibration to yield reliable results and less generically applicable results (Den Bieman et al., 2020). The wide diffusion of machine-learning techniques, instead, led in the last years to numerous and innovative applications of the image processing (e.g., Li et al., 2021). Among others, Stringari et al. (2019, 2021) made use of machine-learning techniques based on the pixel intensity peaks to detect the wave breaking; Buscombe et al. (2020) applied deep learning techniques to estimate wave heights and periods from imagery of waves in the surf zone; Den Bieman et al. (2020) used segmentation algorithms to obtain quantitative measurements of the free surface elevation and of the wave run-up from the video-analysis of physical model tests. These latest studies demonstrate the reliability of the automatic processing of videography, highlighting its effectiveness and advantages with respect to more traditional techniques.

Following the stream of the machine-learning algorithms, this paper investigates the effectiveness and the potentialities of the automatic video-cluster analysis as low-cost and non-intrusive method to model the wave-structure interaction processes in alternative to more traditional or expensive techniques. In particular, the aim of the present contribution is to demonstrate that such technique can be easily and successfully applied to study the wave run-up and wave overtopping phenomena, under wave breaking, high-turbulence and high-aerated flow conditions, providing accurate quantitative estimations of the main overtopping parameters (discharge, volumes, velocities) and, for the first time, quali-quantitative estimations of the air entrainment concentration during the several phases of the wave and flow propagation. To the authors' purpose, the video-records of laboratory tests of wave overtopping at sea-dikes (Formentin et al., 2019a, 2019b, see Section 2) were elaborated with a frame-by-frame cluster analysis algorithm (Section 3) to reconstruct the free-surface elevation signals across the structure profile (Section 4) and to get spatial-time mapping of the areas of the flow subjected to air entrainment (Section 5). Specific pre- and post-processing filtering techniques were also implemented to improve the automatic recognition of the image features (Section 3), outlining a new set of procedures that may represent new state-of-the-art guidelines for the optimization of the automatic cluster analysis. The main results, the potentialities and the limits of the image processing procedure are summarized (Section 6).

2. Description of the tests

2.1. Tested configurations

The videography-modelling technique presented in this contribution was applied to a total of 184 small scale experiments of irregular wave attacks against smooth dike-type structures conducted in the wave flume of the Hydraulic Laboratory of the University of Bologna (Unibo). The experiments consisted of 56 tests of wave run-up and wave overtopping at dikes characterized by a plain, trapezoidal cross-section and 128 further tests of wave overtopping and wave loads against the same dikes upgraded with crown walls, included in correspondence of the on-shore edges.

A wide-angle picture of the wave flume and a front-view picture of the structure with the crown wall installed at the end of the flume are shown in Figure 1.

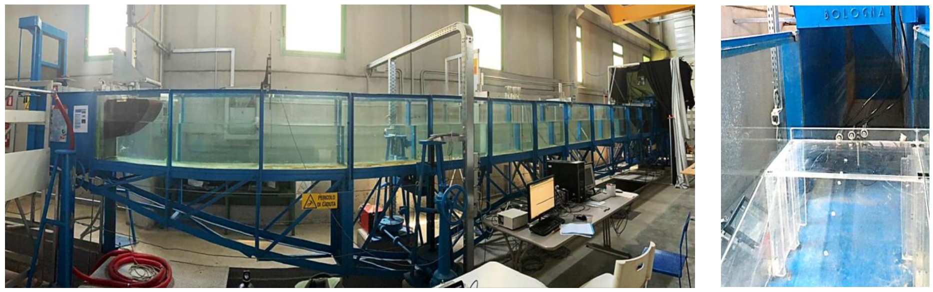

Figure 1. Wide-angle view of the wave flume (left) and front-view of the structure with crown wall installed at the end of the flume (right).

Figure 2 shows the scheme of the cross-section of the tested configurations, providing reference to the symbols and parameters which will be adopted hereinafter. Following the EurOtop (2018) classification of the structure types, and in line with published articles on the Unibo experiments (e.g. Formentin and Zanuttigh, 2019), the crest width of the dikes is hereinafter considered and schematized as a berm (width B, emergence to the swl $h_b<0$).

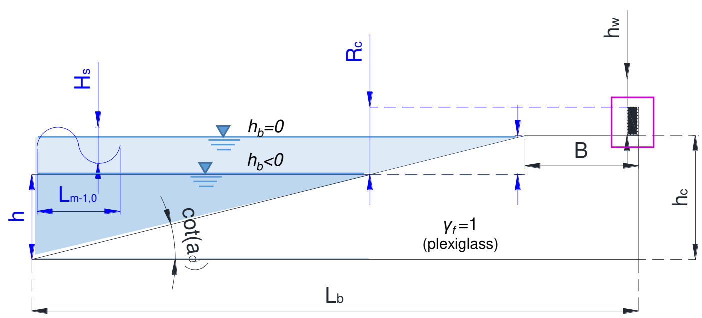

Figure 2. Schematic layout of the tested configurations (not in scale) with reference to the symbols and parameters.

All the tested cross-sections presented the same structure height from the bottom of the channel to the berm level (h_c in Figure 1) equal to 0.35 m and the same distance between the berm off-shore edge and the wave maker (L_b-B) equal to 10.75 m. The range of variations of all the other structural parameters were made varying: dike slope $\cot(\alpha_d)$=2 and 4; berm width B= 0.15 and 0.30 m; berm relative emergence to the wave height, h_b/H_{m0}=0, -0.5 and -1 (this latter case, only for tests without walls); crown wall height h_w=0, 0.04 and 0.05 m.

The plain dike configurations were subjected to 6 target wave conditions realized by varying the significant wave height, H_{m0}=0.04, 0.05 and 0.06 m, and the spectral wave periods $T_{m-1,0}$ to get the 2 target wave steepnesses $s_{m-1,0}$= $H_{m0}/L_{m-1,0}$ = 0.03 and 0.04, where $L_{m-1,0}$ is the wave length calculated from $T_{m-1,0}$. The configurations including also crown walls were instead subjected to 4 wave conditions (H_{m0}=0.05 and 0.06 m and $s_{m-1,0}$=0.03 and 0.04). The wave attacks were all characterized by Jonswap spectra, with a peak enhancement factor of γ=3.3 and consisted of approximately 500-600 waves (according to the target peak wave period, T_p).

The structures were all realized in plexiglass (giving a roughness factor γ_f=1) and the walls (when presents) were deeply clamped in the berm to avoid overturning.

2.2. Laboratory equipment

The wave flume at Unibo, largely described in Formentin and Zanuttigh (2019a) and Gaeta et al. (2020), is 10 m long, 0.5 m wide and 1.0 m deep. It is equipped by a piston-type wave-maker with a special cuneiform shape, which generates the waves by its vertical movements. The scheme of the wave flume, including the installed structures and instrumentation for the present tests is shown in Figure 3.

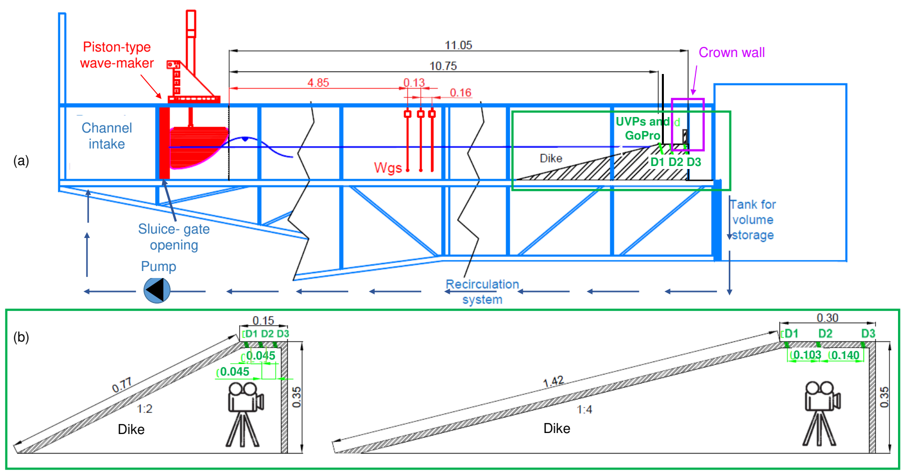

Figure 3. (a) Scheme of the wave flume, structures and instruments installed; (b) particular of the dikes (cot(α_d)=2 and 4), position of the UVPs (D1, D2, D3 in the 2 berms, B=0.15 and 0.30 m) and of the camera Measures in m.

With reference to Figures 1, 2 and 3, the instrumentation adopted in the laboratory consisted of:

- a channel intake – located upstream the wave-maker and separated from the channel by a vertical sluice gate with a small opening at bottom and connected to the recirculation flow – with turbulence dissipation in a still water volume; the system pump-recirculation flow allows to keep the water level difference in the channel within a ±4 mm range for each test.

- a water tank downstream the wave flume and connected to the recirculation conduit, to collect the overtopping volumes and discharge, with a precision in the measure of q of approximately $1 \cdot 10^{-5}$ m^3/s.
- 6 resistive wave gauges (wgs) so installed: the first one in the settling chamber to measure and regulate the recirculation flow; the second one at approximately half wave length ($0.5 \cdot L_{m-1,0}$) from the wave-maker to control the generated free-surface elevation; the following 3 at $\approx 1.5 \cdot L_{m-1,0}$ to separate the incident and reflected waves (the exact position is shown in Figure 3a with red color); the last one in correspondence of the mid-section of the berm width to measure the overtopping layer thickness. The sampling frequency of 100 Hz was selected for all the gauges.
- 3 Ultrasonic Doppler Velocimeters (UVPs) installed along the structure berm to record the time series of the vertical profiles of the horizontal flow velocities u and track the free surface elevation h. The positions of the three UVPs, shown in Figure 2b in green color and referenced as D1, D2 and D3, were selected to reconstruct the statistics of h and u in proximity of berm off-shore edge (D1), in the berm mid-section (D2) and close to its in-shore edge (D3).
- a 30 Hz full-HD camera (resolution 1080x1920 pixels) employed to film the wave run-up, the flow over the crest, the overtopping process and the wave impacts at the walls (when present); the camera was placed at the exactly perpendicular position to the side window of the wave flume where the dike was located, see Fig. 3b; a "darkroom" was set up around the channel in correspondence of the camera – visible in Figure 1 to the right – to optimize the light condition for filming.

2.3. Laboratory measurements

The following "direct" measurements were performed during the experimental tests:

- the time series of the free-surface elevations (h) at the wgs installed in the channel;
- the average specific wave overtopping discharges (q_{tank}, $m^3/(ms)$) calculated from the volumes stored in the tank;
- the time series of the overtopping flow characteristics (depths h and velocities u) over the berm from the records of the 3 UVPs;
- the records of the experiments filmed with the full-HD camera.

From the elaboration of the "direct" measurements, the following further results are available:

- significant incident wave heights (H_{m0}) in front of the structures and bulk wave reflection coefficients (K_r);
- the instantaneous overtopping wave volumes for unit width (V, m^3/m) from the integration of the h-signals in the time-domain recorded at D1, D2 and D3 from the reflecting water-air interface of the projected acoustic beams;
- the average specific overtopping discharges, q_{Vol} ($m^3/(m\ s)$) at D1, D2 and D3 obtained as sum of the corresponding instantaneous V-values to the duration of the test (480 s);

- the wave celerities (*c*), the celerities of propagation of the water front above the berm width, from the coupling of the UVPs records of the *h*-values at D1 an D3; for each wave overtopping the berm, the instantaneous wave celerity is calculated as the ratio between the known-distance between D1 and D3 (*diswg*=0.090 and 0.243 m for *B*=0.15 and 0.30 m, respectively, see Figure 3b) and the corresponding time lag between detected h wave peaks at D1 and D3;
- the specific overtopping discharges, q_{cel} ($m^3/(m\ s)$) calculated from the integration of the wave celerities *c* with the water depths *h*; for shallow water conditions, under the hypothesis of kinematic wave propagation, flow velocities and wave celerities can be assimilated.

The ranges of the main parameters resulting from the experiments are reported in Table 1, where:

- $\xi_{m-1,0}$ is the Iribarren-Battjes breaker parameter resulting from the values of the spectral wave height (H_{m0}) and spectral wave length ($L_{m-1,0}$) measured at the toe of the structure;
- R_c/H_{m0} is the structure relative freeboard (considering the crown wall height) as measured in the lab, i.e. accounting for the mean swl in the wave flume during the test; the negative values of $R_c/H_{m0}<0$ (tests on dikes without walls only) are obtained when the mean swl increased during the test, giving a slightly submerged berm level;
- the symbol "*" following the q_{tank}-values (tests with walls) indicates that the value reported in the Table is the minimum non-zero value, whereas some tests actually gave no overtopping (q_{tank}=0);

Table 1. Ranges of the main parameters resulting from the experiments. The symbol "*" indicates that the minimum non-zero value is reported.

	$\xi_{m-1,0}$	R_c/H_{m0}	q_{tank} [m³/sm]
# tests without wall (h_w=0)	[1.19; 3.72]	[-0.19; 1.12]	[1.90e-4; 5.00e-3]
# tests with wall	[1.23; 4.03]	[0.66; 2.51]	[1.09e-5*; 7.00e-4]

Further reference to the laboratory measurements and results can be found in: i)Formentin and Zanuttigh (2018) and Formentin and Zanuttigh (2019a) for the characterization of the data of *q*; ii) Formentin et al. (2019a) and Gaeta et al. (2020) for, respectively, the presentation of the overtopping flow processes across the berm (data of *h*, *u* and V) and a detailed description of the elaboration technique of the data from the UVPs; iii) Formentin and Zanuttigh (2019b) as regards the wave coupling technique, the wave celerities and related quantities (e.g., q_{cel}).

2.4. Characteristics of the selected tests

The accuracy of the image processing methodology is assessed in Section 4 by showing the results of the cluster analysis applied to the reconstruction of the free-surface elevation for 8 tests selected among the whole database.

The selected tests, whose characteristics are reported in Table 2, cover the variety of the geometrical configurations tested in the laboratory (the 2 slopes, cot(α_d)=2 and 4; the 2 berm relative submergences h_b/H_{m0}=0 and-0.5 and the 2 berm widths, B=0.15 and 0.30 m). The 2 slopes were selected to specifically investigate the results of the procedure under both breaking (cot(α_d)=4) and non-breaking (cot(α_d)=2) wave conditions, as determining completely different run-up and overtopping flow processes.

The wave conditions are the same for all the 8 tests (target wave height H_s=0.05 m and target wave steepness $s_{m-1,0}$=0.03) and all the configurations refer to structures without walls. For these tests, the main overtopping flow characteristics were by elaborating the free-surface elevation signals recorded at virtual gauges conveniently set up above the structure berm (Sub-section 4.1). The "virtual" overtopping flow characteristics are then compared to the corresponding quantities measured in the lab from "traditional" techniques (Sub-sections 4.2 to 4.4).

Table 2. Summary of the 8 experiments elaborated with the video-cluster analysis.

Test ID	Test ID	cot(α_d) [-]	B [m]	h_b/H_{m0}
R00H05s3B30c2	TD1	2	0.30	0
R00H05s3B15c2	TD2	2	0.15	0
R05H05s3B30c2	TD3	2	0.30	0.5
R05H05s3B15c2	TD4	2	0.15	0.5
R00H05s3B30c4	TD5	4	0.30	0
R00H05s3B15c4	TD6	4	0.15	0
R05H05s3B30c4	TD7	4	0.30	0.5
R05H05s3B15c4	TD8	4	0.15	0.5

3. Description of the methodology

This Section describes the image-processing methodology developed to reconstruct a series of parameters and data related to the wave overtopping and the wave impact processes from the analysis of the video-records of the experiments conducted at Unibo. The methodology is based on the cluster analysis of the frames and on the automatic extraction of "features" from the images and includes a number of pre- and post-processing techniques specifically designed to improve the automatic detection phase. The image clustering technique, which was originally used by Gaeta et al. (2020) to reconstruct the water depth at dike crest, has been upgraded to meet the following objectives i) tracking the free-surface of the water along the slope and above the berm; ii) reconstructing the shape and the height of the up-rushing jet along the wall during the impact events; iii) estimating the amount of air bubbles entrapped in the overtopping flow and beneath the water tongue during the impacts.

The open-source toolbox "PRTools" (Pattern recognition Tools, http://prtools.tudelft.nl/?from=www.website80.com; Duin and Pekalska, 2015) developed by TU Delft was adopted for the cluster analysis and the features extraction from the videos.

All the implemented algorithms and the image filtering techniques are tuned to fit the specific site conditions, the camera characteristics (resolution, frequency of acquisition, etc.) and the environmental features (light, blur, channel shape and size, etc.). However, the ensemble of the methodology might represent a "best practice" exportable to other applications related to the image processing of video-records of experiments on coastal structures.

The main steps composing the methodology are illustrated in the following Sub-sections.

3.1. Calibration

The first step prior to any image processing consists in the camera calibration. This step is necessary to evaluate and correct the image distortion due to the camera lens and to extract the information required to convert the data minable from the images from the camera intrinsic coordinate system (pixels) to world points (m). The camera calibration requires a specific video to be performed after each power on of the camera and before starting filming the experiments. The resolution and the size of the calibration video must be the same set up to record the experiments.

The calibration of the camera was performed following the approach indicated by Bouget (2015) (see Figure 4): a planar checkerboard was moved in front of the camera in correspondence of the structure in the wave flume. A few images presenting the checkerboard in different positions with respect to the structure were taken. The intrinsic coordinates (pixels) of the corners of the squares are automatically detected (red dots in Figure 4c) and the corresponding world coordinates are generated (Figure 4b) by knowing the metric extrinsic size of the checkerboards (30 mm). Finally, the camera calibration parameters are calculated: the rotation translation matrix and the translation vectors to be used to convert all the data from the videos of the experiments from intrinsic to world coordinates. The camera calibration process involves the evaluation of the skewness and of the tangential distortion and returns the estimation of the mean projection error per image (Figure 4b) due to lens distortion, optical errors and 2D–3D projections. In the example of Figure 4b such error ranges approximately between 1 and 2.5 pixel per image, i.e. between 0.3 and 0.75 mm. Generally, it was verified that the projection error was always less than 1 mm per image.

To evaluate the accuracy of the calibration process before carrying out and filming the experiments, it is suggested to select a sample frame for validation. By comparing the main geometrical distances (e.g., width of the berm or slope angle of the dike) of the picture to the corresponding real dimensions, the relative errors characterizing the conversion process can be computed. In the present application, relative errors between 0.6 and 2% were found for the lengths and between 0.5 and 2.5% for the slope angles.

Once calibrated the camera, it was possible to run and film the experiments. For each set of tests performed after each power on of the camera, the same calibration parameters, conversion factors and projection errors were assumed.

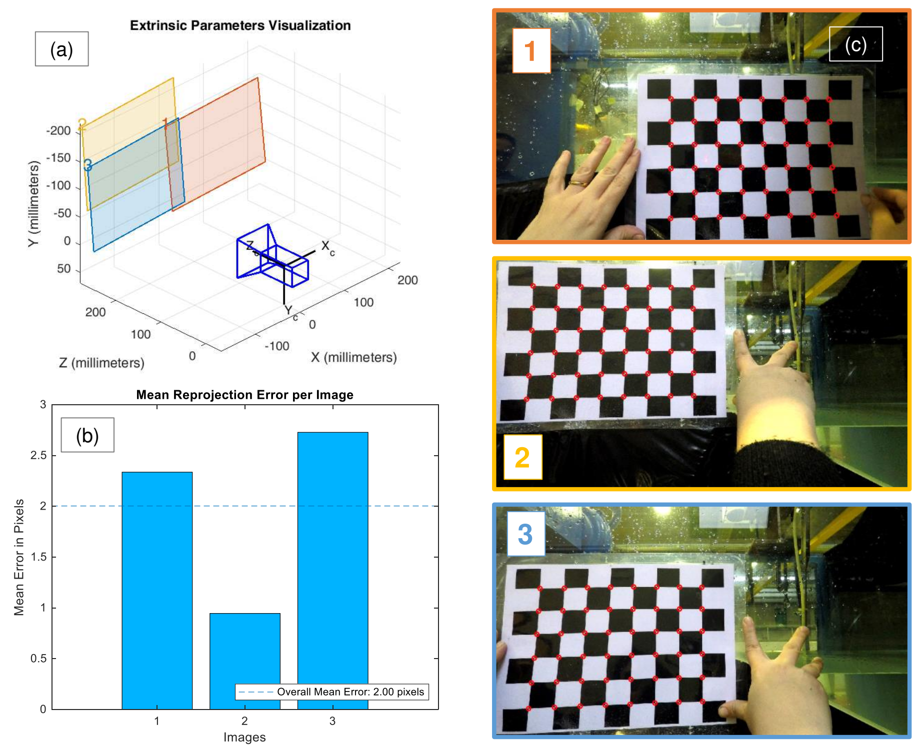

Figure 4. (a) Extrinsic camera visualization (world coordinates) of the 3 images used for the calibration; (b) mean camera projection error per image (pixels); (c) images (1-3) used for the camera calibration and checkerboard points (red dots) automatically detected.

3.2. Pre-clustering optimization techniques

The pre-clustering techniques were designed to improve the accuracy of the automatic detection of the different objects (water, air entrainment, structure, etc.) as much as possible. The following techniques were applied to each frame of each video and in the following order.

i) Image subtraction: the first frame – representing the structure in the channel and the initial swl conditions before running the waves and named "frame 0" hereinafter – was subtracted from each frame of the record. Subtracting an image from another image means subtracting, pixel by pixel, the digital numeric value of the second image from the first one. This process allows levelling uneven sections of an image, such as shadows, reflexes or blurs, and removing all the fixed elements present in all the frames (for example, the shape of the structure or the border of the walls of the channel). After the subtraction, only the elements differing from the "frame 0" are kept, i.e. the water and its evolution.

ii) Conversion into grayscale, to reduce the size of the image avoiding redundant information stored in the color-scale picture. The use of grayscale images is also recommended to ease the pattern recognition step and for the application of the functions related to the image adjustment (i.e. noise add, light and contrast adjustment, application of morphological filters, etc.).

iii) Noise add: when large portions of the images result too uniform for the pattern recognition, the training of the cluster model fails. The application of a Gaussian white noise is useful to solve this shortcoming. In the present case, a Gaussian noise with a mean of 0 and a variance from 0.001 to 0.003 was applied. The variance values should be tuned for each set of experiments filmed after the same camera power-on through a trial-and-error process commanded by the cluster training phase. The more uniform the images, the higher the variance of the noise to be included.

iv) Enhancement of the contrast of the grayscale image using a contrast-limited adaptive histogram equalization (uniform histogram with a contrast enhancement limit = 0.03).

Figure 5a shows an example frame as taken from the camera, while Figure 5b shows the same picture as resulting from the application of the pre-processing techniques.

3.3. Image clustering

The clustering is the task of grouping different "objects" (or patterns) of a picture into clusters so that the objects in the same group are more "similar" to each other than to those in other groups (clusters). An ideal clustering would recognize, for example, all the pixels composing the water as actually belonging to the same cluster. An automatic clustering can detect patterns (similarities among objects) in the images that are "invisible" to the human eye and extract quantitative information otherwise hardly accessible (e.g., estimate the amount of air entrapped in the water phase).

Numerous clustering algorithms are available and several categorizations can be done upon different aspects (Duda et al., 2012). In the present study, the image clustering was performed with the toolbox PRTools by selecting the Expectation–Maximization (EM) algorithm (Dempster et al., 1977): it is an unsupervised, probabilistic, iterative method to partition data into clusters based on maximizing the likelihood to find the statistical parameters of underlying subpopulations in the dataset. Once defined the total number of clusters, the EM algorithm classifies the objects into temporary clusters (E step), which are re-assigned iteratively after the evaluation of the "similarity" (or distance) of the objects within the same cluster (M step). The iterations may stop after a certain number of attempts (early stopping) or when the subdivision of the objects into clusters is stable, i.e. when an object is definitely assigned to a cluster. The EM algorithm performs a partitioning clustering and, requiring the *a priori* definition of the number of clusters, relies on the analyst's knowledge to classify the clusters in a meaningful way. According to the syntax of PRTools, the labeling "crisp" was selected to apply a boosted version (generalized *k-means* algorithm) of the traditional EM algorithm.

To perform a cluster analysis of a video record, it is necessary to train a cluster model map, i.e. to create an example of clustering of the objects composing a frame to be used as reference (model map). The frame selected for the training must be representative of all the frames of the record and, in particular, must include all the clusters of objects that may appear in a frame (water, solid structure, air entrapment, etc.). The number of clusters to be identified in each frame depends on the image quality (e.g., light exposure, flow patterns over the crest, drops on the walls of the channel), on the expected turbulence level and – in general – on the objective of the analyses. The summary of the features selected for the training of the cluster models is reported in Table 3.

The analysis of the experiments on dikes without walls were focused on the tracking of the free surface only, disregarding the analyses of the areas of the flow affected by air entrainment. For these tests, the frames for the training were therefore selected to reproduce an instant of wave overtopping characterized by a pseudo-steady overflow process and no (or modest) turbulence and no bubbles. A number of 2 clusters was setup for the training of the cluster model map, which basically corresponds to the objects "water" and "non-water". The edges of such clusters represent the interfaces water-structure and water-air, and this latter one can be directly taken as free-surface. An example of a frame selected for training is shown in Figure 5a (original picture). The cluster model map of this frame returned with the training is shown in Figure 5c: here, the 2 clusters are clearly distinguished and the free-surface interface is sharp.

On the contrary, the video-analysis of the experiments on dikes with walls was also aimed at tracking the profile of the water jets along the walls and at detecting the areas of the flow more frequently subjected to turbulence and air entrainment. To this purpose, the training frames were selected among images representing a fully-broken wave propagating above the berm, characterized by a high air entrainment rate. An example of training frame is reported in Figure 6a. This example shows that the bi-phase flow is characterized by different shades of color and brightness. To "capture" all the different shades and to correctly cluster all the area of bi-phase flow as such, it was necessary to define "redundant" clusters of objects. Specifically, 5 clusters were set up for the experiments on walls to ideally group the image objects into the classes "water", "structure" and "air entrainment", where the latter class "air entrainment" was expected to appear into up to 3 clusters. The association cluster-objects varied for each experiment, because each experiment requires the training of a specific cluster model map, and the training is a random, iterative process that vary at each run. Figure 6b shows the trained cluster model map of Figure 6a: in this map, the areas of the flow that may be concerned by air entrainment correspond to the clusters 3 and 5 (light blue and yellow, respectively). For other experiments, 3 clusters were necessary to correctly detect the areas with air.

Independently of its level of complexity, the association cluster-objects relies on the human supervision in the end. All the cluster model maps must be interpreted by the human intelligence after the training to associate one object to one (or more) clusters.

Table 3. Summary of the features adopted for the cluster training.

Dataset	Training algorithm	Number of clusters	Analyses performed (features)
# tests without wall	EM-crisp	2	free-surface tracking
# tests with wall	EM-crisp	5	free-surface tracking; bi-phase flow area estimation; wave-impact reconstruction (analysis in progress)

3.4. Post-clustering optimization techniques

After the image-clustering, the frames are transformed into cluster maps similar to the examples of Figures 5c or 6b, where each pixel is associated to a label. Post-clustering techniques were designed to convert the information embedded in the cluster maps of the frames into data for further elaboration.

3.4.1. Free surface tracking

For the free-surface tracking and the reconstruction of the shape of the water jet during the wave impacts at the walls, the following post-clustering techniques were applied.

i) Segmentation of the areas of the image automatically labelled as "water": the segmentation returns a binary image containing 1 where the function finds edges and 0 elsewhere. The selected image detection method is based on the "Canny" algorithm (Canny, 1986). Figure 5d shows in red the edges of the "water" resulting from the segmentation of one frame relative to a test on dikes without walls. In Figure 5d, the contour of the free-surface is correctly detected, though several, unwanted areas of the frame (drops on the walls of the flume or other disturbing elements) have been wrongly labelled as "water", as marked by the red contour.

ii) To reduce the number of gaps in the edge of the free-surface, the filling of the "holes" procedure was performed.

iii) To remove the disturbing elements, an ad hoc filter based on the area of the "connected components" of the image was designed: this filter removes all the connected components that have fewer than 200 pixels, where 200 is approximately the largest realistic area of the drops on the walls. The preliminary operation of holes filling (ii) ensures that all (or most) of the adjacent pixels composing the edge of the free-surface are connected and that the "water" is not removed by the filter.

iv) To remove specifically-shaped disturbing elements in the images "survived" to the extraction of the connected components, the "morphological filtering" was applied. In a morphological operation, each pixel of the image is adjusted based on the value of other pixels in its neighborhood. By choosing the size and shape of the neighborhood, it is possible to construct a morphological operation that is sensitive to specific shapes in the input image. The following 2 morphological operations were built: 1) elimination of all the parts of the figure containing a vertical element of at least 4-pixel length (image erosion), to remove the edges of the walls of the channel or of the wires; 2) dilation of all the parts of the figures containing a horizontal element at least 5 pixel-long (image dilation) to enhance and connect the edges of the berm. The result of the subsequent holes filling, extraction of the connected-components and morphological filtering of the edges of the "water" is shown in Figure 5e. In this Figure, it is possible to detect all the edges removed from the original output of the image clustering and segmentation (Figure 5d) and the marked profile of the structure berm.

v) Automatic procedure for the free-surface tracking. An if-else, customized procedure was developed to reconstruct the effective profile of the free-surface, abscissa after abscissa, from the dike slope to the wall height (when present), disregarding the edges of all the remaining objects improperly classified as water and which were not eliminated by the procedures ii) to iv). Such procedure is based on the definition of an initial time condition and follows a sort of "forward scheme" to identify the nearby points of the free-surface, based on the assumption of the continuity of the free-surface profile itself. The initial condition is the actual profile of the free-surface of the first frame, which is prompted by the direct, human identification of the coordinates through a graphical user interface. The initial condition is used for comparison for the following frame: for each abscissa, the ordinate of the edges of the "water" is kept as free-surface of the current frame if it is "sufficiently" close (± 10 pixels) to the corresponding ordinate of the initial condition. The free-surface is updated for the current frame and is used for comparison for the following one, and so on. When no value of the edge of the "water" of the current frame is sufficiently close to the value of the free-surface at the same abscissa of the previous frame, a comparison among adjacent pixels of the current frame is performed (forward scheme). Starting from the left-most abscissa (wave inlet), the ordinate of the nearby pixel of the "water" edges is kept if sufficiently close (± 10 pixels) to the ordinate of the previous abscissa, otherwise it is discarded. If no points are accepted for a certain abscissa, a value of "NaN" is assigned for that position. The "NaNs" correspond to holes in the profile of the free-surface. The value of ± 10 pixels was set after a trial-and-error procedure and based on the time sampling frequency of the video (30 Hz) and the spatial resolution of the frame (1080x1920 pixels).

vi) Filtering. Median-filters and adjacent-pixel-filters were designed and applied to the records of the free-surface as resulting from step v) to fill the holes (NaNs) and smooth the free-surface profile, removing spikes and discontinuities. The time series of the filtered free-surface elevation values, for the whole duration of the video, is the final output of the post-clustering techniques applied to each test. Figures 5f and 6c display the filtered free-surfaces (blue crosses) for the corresponding frames. The comparison between Figure 5d and Figure 5f shows the effects of the application of the steps i)-vi) to the outputs of the cluster analysis.

3.4.2. Bi-phase flow area detection

The detection of the areas of the flow subjected to entrainment of air bubbles was performed for the experiments on walls only, through the application of the following post-clustering techniques.

i) Segmentation of the areas of the image labelled as “air entrainment”. With reference to the example of Figure 6b, the areas belonging to the clusters 3 and 5 were labelled as “air entrainment” upon eye examination of the cluster map.

ii) Extraction of the connected components to clear up the areas of “air entrainment” from all the connected components consisting of less than 20 pixels of area extent (small drops escaped from the image subtraction).

iii) Morphological filtering of all the mono-dimensional, 10-pixel-length features, to remove the elements composing the contour of the structure which were wrongly assigned to the “air entrainment” clusters because their intensity was similar to the one characterizing the bi-phase flow.

iv) If-else, loop-procedure for the actual estimation of the areas of the flow potentially concerned by air entrainment. Such procedure processed, abscissa after abscissa, all the pixels labelled as “air entrainment” survived to the filtering procedures. Each pixel was accepted as a potential air-element if its ordinate was lower than the ordinate of the water free-surface for the same abscissa. Therefore, the detection of the bi-phase flow areas is necessarily posterior to the free-surface tracking.

The example of Figure 6c shows in red the contour of the areas of the flow characterized by air entrainment as returned after the application of the steps i)-iv). The eye analysis of this picture confirms that these areas do actually correspond to the areas of the flow affected by air entrainment. The eye-examination of tens of frames randomly selected from the video records of the tests under different light and wave attack conditions has confirmed that the procedure detects the areas of bi-phase flow with the same accuracy shown in Figure 6c.

The main application of the bi-phase flow detection analysis was the estimation of the percentage of the water flow affected by air entrainment. Such percentage was calculated for each frame of each experiment, by dividing the extent of the areas of air entrainment to the total area of the flow, estimated as the extent of the convex hull of the object “water” (green line in Figure 6c). The details of the air entrainment analysis are illustrated in Section 5.

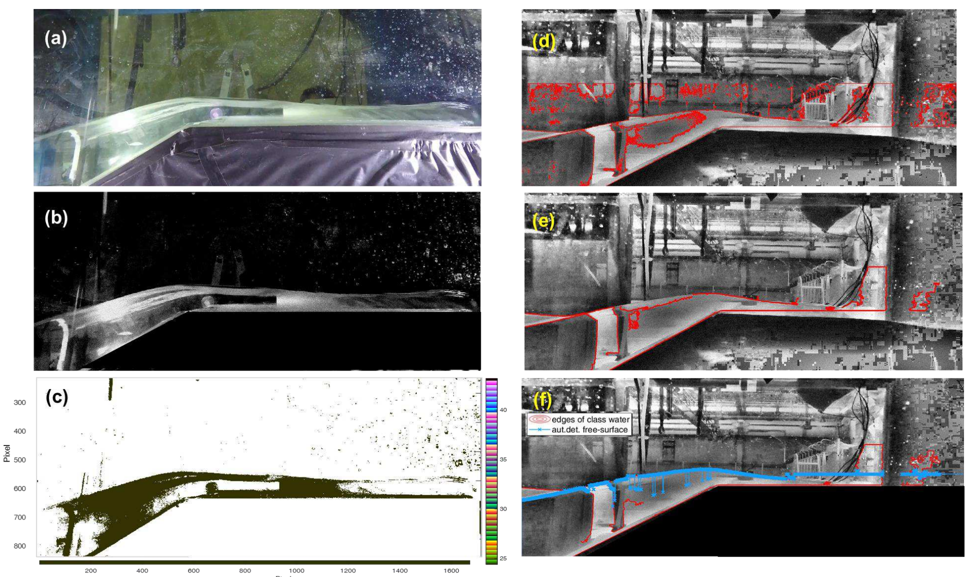

Figure 5. a-b-c) Example frame selected for training the cluster model for a test without wall: a) Image as taken from the camera; b) image as resulting after the application of the pre-processing techniques; c) clustered-model map of the image. d-e-f) Example frame processed with the cluster analysis: d) edges of the cluster "water" resulting from the image segmentation (red); e) edges of the cluster "water" (red) after the application of the post-clustering techniques; e) profile of the free-surface elevation as result of the whole image processing procedure (blue).

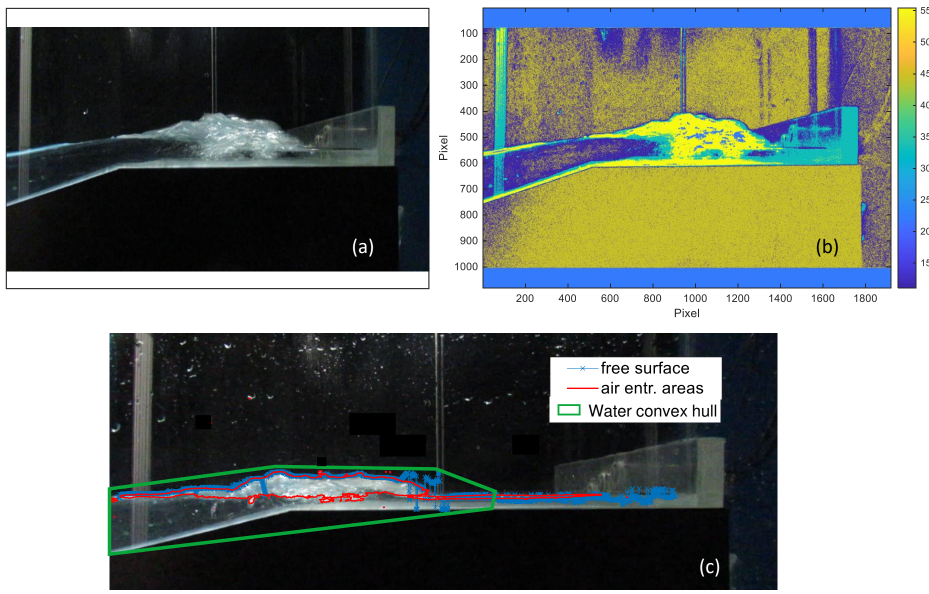

Figure 6. a-b) Example frame selected for training the cluster model for a test with wall: a) image in real-scale colours and light conditions as taken from the camera; b) clustered-model map of the image. c) Example frame processed with the cluster analysis showing: the profile of the filtered free-surface elevation (blue); the contour of the object “air” (red) after the application of the post-clustering techniques; convex hull of the object “water” (green).

4. Results and validation of the methodology

4.1. Image elaboration and creation of the virtual gauges

To elaborate the results of the videography for each of the tests reported in Table 2, it is firstly necessary to convert the values of the free-surface elevations resulting from the video analysis from pixels to "real world" coordinates. The conversion is carried out based on the parameters of calibration of the camera (see Sub-section 3.1).

2 "virtual gauges" were defined to extract the time series of the overtopping flow depths (*h*) in correspondence of the off-shore (OE) and in-shore (IE) edges of the berm and, specifically in correspondence of the position of the UVPs, D1 and D3 (see Figure 3b). These time series were elaborated to derive the statistics of practical interest (mean, standard deviation, upper-2% percentiles, $h_{2\%}$, maximum envelopes), to reconstruct the individual overtopping volumes (V), to calculate the wave celerities (*c*) and to estimate the average and instantaneous wave overtopping discharges (*q*). The comparison among these quantities and the corresponding measurements from the lab is used to verify the accuracy of the results of the videography analysis and assess their uncertainty (Sub-sections 4.1.1 to 4.1.3). Figure 7a illustrates, for an example frame, the position of the virtual gauges and Figure 7b provides 2 exemplary time series of the *h*-values reconstructed at the 2 virtual gauges from the video-cluster analysis.

The quantities *c*, *V* and *q* were calculated from the time series of the *h*-values by applying the procedure of threshold-down-crossing and wave-coupling developed by Formentin and Zanuttigh (2019b). This procedure was applied to both the virtual signals and the records of the UVPs. The procedure consists in the identification of the individual overtopping events based on the definition of thresholds (shown as circles in Figure 7b) and in the coupling of the events at the 2 gauges based on the comparison of the shape of the *h*-signals and on the time lag occurring to an event to propagate from the first to the second gauge, knowing the distance between the 2 gauges (*diswg*) themselves. An overtopping event is identified in the time domain by 2 consecutive crossings of a threshold (namely, t_i and t_{i+1}). By integrating the *h*-signal between t_i and t_{i+1}, it is possible to calculate the volume (V_i) of each i-th overtopping event:

$$V_i=\int_{t_i}^{t_{i+1}} h(t)\, dt, \quad [\mathrm{m^3/m}] \tag{1}$$

The sum of the individual volumes for the whole duration of the experiment, gives the total volume of wave overtopping, V_{tot}:

$$V_{tot}=\sum_{i=1}^{Now} V_i, \quad [\mathrm{m^3/m}] \tag{2}$$

where *Now* is the number of overtopping waves (i.e. of the overtopping volumes). By dividing V_{tot} for the duration of the experiment (480 s), it is possible to estimate the "volumetric" average specific wave overtopping discharge, q_{vol}:

$$q_{vol}=\frac{V_{tot}}{t_{tot}}, \quad [\mathrm{m^3/(s \cdot m)}] \tag{3}$$

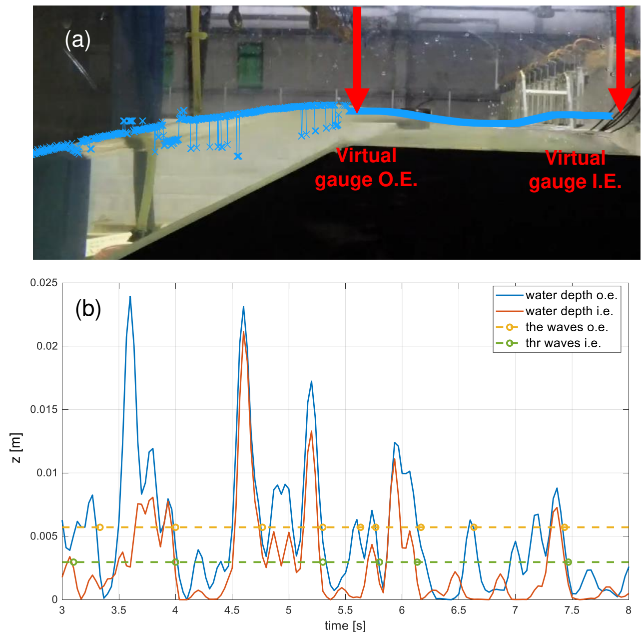

Figure 7. a) Definition of the "virtual gauges" for the extraction of the overtopping flow depths, *h*, from the videography. The blue crosses represent the free-surface as resulted for this example frame after the application of the filtering techniques. b) Example time series of the overtopping flow depths (*h*) at the 2 virtual gauges (blue, OE edge; orange IE edge). The yellow and green dashed lines are the threshold for the wave detection at the o.e. and i.e., respectively.

The quantities V_i, V_{tot} and q_{vol} can be calculated for each test and for both the virtual gauges. The comparison between the corresponding quantities at the 2 virtual gauges is used as evidence of the mass conservation. The same quantities are also compared to the corresponding results from the elaboration of the UVPs signals (see Sub-sections 4.3 and 4.4).

The wave coupling performed by the procedure of Formentin and Zanuttigh (2019b) associates the instants of threshold-down-crossing of each overtopping event detected at the 2 virtual gauges (and at the 2 UVPs D1 and D3) namely t_{i1} for the virtual gauge at the OE and t_{i2} for the virtual gauge at the IE. Given *diswg*, it is possible to calculate the celerity of propagation of each overtopping event:

$$c_i = \frac{diswg}{t_{i2} - t_{i1}}, \qquad [\text{m/s}] \tag{4}$$

For each experiment, the mean, the maximum and the upper 2%-values of *c* can be derived from the statistical analysis of the c_i-values. The wave celerities can be used, to some extent, as estimators of the overtopping flow velocities *u* (Formentin and Zanuttigh, 2019b).

Finally, the celerities can be used to estimate the values of the wave overtopping discharges of each overtopping event ($q_{cel,i}$) and the average overtopping discharges (q_{cel}):

$$q_{cel,i}=c_i\cdot\frac{\int_{t_i}^{t_{i+1}} h(t)\,dt}{t_{i+1}-t_i}, \qquad [m^3/(s\cdot m)] \tag{5}$$

$$q_{cel}=\frac{\sum_{i=1}^{Now} q_{cel,i}}{t_{tot}}, \qquad [m^3/(s\cdot m)] \tag{6}$$

where the second term on the right-side of Eq. (5) is the time-average of the *h*-values of the i-th overtopping event. The average q_{cel} can be compared to q_{Vol} (both the quantities from the videography and from the UVPs) and to q_{tank} (see Sub-section 4.2 and Figure 8).

4.2. Overtopping flow characteristics

Figure 8 illustrates the comparison among the values of $h_{2\%}$ at the OE and IE as resulting from the measurements of the UVPs in the lab (abscissas) and from the videography (ordinates) for the tests TD1-TD8 of Table 2. The average relative errors among the videography and the UVP values of $h_{2\%}$ are +4.1% and +36% for the OE and the IE respectively. In both cases, the positive sign indicates that the videography tends to give higher estimations of the overtopping flow depths than the UVPs. The modest error at the OE actually indicates a very good agreement among the results from the 2 techniques, while the higher uncertainty at the IE can be explained with the single outlier of Figure 8 relative to the test TD2 (relative error +90%). It was verified that the cause of the outlier is related to the particularly bad lighting conditions affecting the quality of the video records, especially in correspondence of the outlet of the wave flume (i.e. closer to the IE).

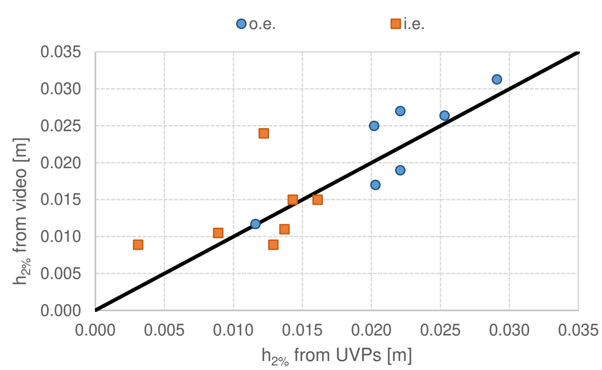

Figure 8. Values of $h_{2\%}$ at the OE (blue circles) and IE (orange squares) measured in the lab with the UVPs (abscissa) and reconstructed from the cluster analysis of the video of the experiments (ordinate). Tests TD1-TD8 of Table 2.

4.3. Overtopping discharge

Figure 9 provides the comparison among the values of q measured in the water tank in the lab (q_{tank}, abscissa) and the corresponding estimations derived from the videography for the tests TD1-TD8. In this Figure, the triangles and the diamonds represent the values of q calculated from, respectively, the overtopping volumes (q_{vol}) and the wave celerities (q_{cel}). The agreement among the videography and the water tank values is quantified by the relative errors +19% and -25% in case of q_{vol} and q_{cel}, respectively. Whereas the absolute value of the errors is similar, the signs reveal that q_{vol} and q_{cel} tend to respectively overestimate and underestimate the overtopping discharges.

Similarly to the case of $h_{2\%}$ of Figure 8, the average overestimation observed for q_{vol} is induced by the single outlier relative to the test TD2, clearly visible in Figure 9 (relative error +78%). On the contrary, the underestimation trend associated to q_{cel} is observed for almost all the tests, and in particular when q_{tank} >3*10^{-3}. These underestimations are probably due to the higher level of complexity of the procedure necessary to extract the q_{cel}-values with respect to q_{vol}, involving the coupling of the overtopping events between the 2 virtual gauges. It is likely that some of the waves propagating faster between the OE and the IE are not caught by the video recording at 30 Hz. Indeed, Figure 7b shows that the time-lag between the records of h at the OE and at the IE is generally very small and, in some cases, the overtopping events identified at the OE are nearly coincident to the events identified at the IE (compare, for example, the peaks of the events recorded at the 2 virtual gauges around 4.6 and 5.2 s). The upper limit in the wave coupling is imposed by the Nyquist frequency, which is one-half the recording frequency, i.e. 15 Hz. Since 2 frames are necessary to perform the wave coupling, the upper-limit is reduced of a further one-half. Eventually, the maximum wave celerity that can be caught by the video record can be evaluated as follows:

$$c_{max}=\frac{\text{acquisition frequency}}{4}\cdot diswg. \tag{7}$$

For the Unibo experiments, c_{max}=7.5·$diswg$ = 0.675 m/s in case of B=0.15 m ($diswg$=0.09 m, see Fig. 3b) and 1.82 m/s in case of B=0.30 m ($diswg$=0.243 m). As shown in Formentin et al. (2019), the maximum wave celerities values calculated from the coupling of the signals at the UVPs were around 1.2 m/s. Therefore, the limit of c_{max} mainly affects the tests with B=0.15 m.

The limit by Eq. (7) affects in turns, the values of the overtopping discharges q_{cel}, which depends on the c-values Nonetheless, Figure 9 shows that the q_{cel}-values follow the same trend of q_{tank}, revealing that the elaboration of the video records works in principle, and the limit is given by the camera frequency of acquisition. Based on Eq. (7), to perform the wave coupling and estimate the related derived quantities, it can be recommended to set the minimum value of the frequency of acquisition of a camera as follows:

$$(\text{acquisition frequency})_{\min}=4\cdot\frac{c_{max}}{diswg}. \tag{8}$$

For the Unibo tests, being the observed c_{max}≈1.2 m/s, (acquisition frequency)$_{min}$≈50 Hz for the most severe condition of *B*=0.15. In case the condition imposed by Eq. (8) cannot be addressed, it is recommended to prefer the estimations of *q* from q_{vol} rather than q_{cel}.

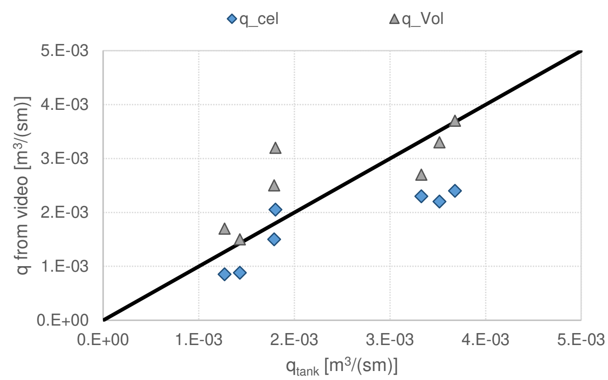

Figure 9. Values of *q* (ordinate) reconstructed from the cluster analysis of the video of the experiments and measured in the water tank of the lab (abscissa). The blue diamonds refer to the q_{cel} values, while the grey triangles refer to the q_{vol} values. Tests TD1-TD8.

4.4. Overtopping volumes

The results of the analyses of the overtopping volumes extracted with the videography are reported in Tables 4 and 5 and in Figure 10.

For each of the tests TD1-TD8, Table4 provides the comparison among the q_{Vol}-values at the OE and at the IE, the relative error between the quantities, the average relative error (μ) and the relative standard deviation ($\sigma_{\%}$) characterizing the distribution.

The results of Table 4 show that the q_{Vol}-values calculated at the OE and at the IE differ on average of -14%, with a standard deviation $\sigma_{\%}$=28%. In most cases the higher estimations of *q* are derived at the OE: this slight decay of q_{Vol} is explained with the decay of the overtopping flow depths *h* along the berm, which is quantified of ≈30-40% (see Figure 8) and which is in line with the expectations from the literature. The EurOtop (2018) manual indeed indicates that "the flow thickness *h* decreases of approximately 1/3 with respect to the value at the off-shore edge". Hence the results of the videography fulfill the continuity equation, because the variations of q_{Vol} are due to the physical evolution of the *h*-values and not to a shortcoming of the methodology.

Table 4. Values of q_{vol} calculated from the videography at the OE and IE for the same tests and corresponding relative errors; average relative error (μ) and relative standard deviation ($\sigma_{\%}$).

Test	q_{vol} OE [m^3/(sm)]	q_{vol} IE [m^3/(sm)]	rel. err. [-]
TD1	3.70E-03	2.70E-03	-0.27
TD2	3.30E-03	2.50E-03	-0.24
TD3	3.20E-03	3.30E-03	0.03
TD4	2.50E-03	2.40E-03	-0.04
TD5	2.70E-03	2.20E-03	-0.19
TD7	1.70E-03	1.50E-03	-0.12
TD8	1.50E-03	1.31E-03	-0.13
μ			**-0.14**
$\sigma_{\%}$	**0.28**		

Table 5 and Figure 10 refer to the single test TD4 and compare the results from the videography to the elaborations of the data from the UVPs and (when possible) from the water tank.

Figure 10 reports in a bi-logarithmic chart the probability distributions of the *V*-values reconstructed from the cluster analysis (blue circles) and from the water-air interface as detected by UVPs (grey triangles). According to the literature, the distributions of the *V*-values can be approximated with a Weibull's function, characterized by the shape factor *b*. Following Formentin and Zanuttigh (2019b), the values of *b* were calculated as the slope of the linear fitting of the higher 20% overtopping. The 2 distributions present very similar shapes and almost the same changes of slope. In both cases, the 2 lower volumes are similarly detached from the main tend and the same consideration applies for the upper tail of the distributions.

Table 5 reports the number of overtopping waves (*Now*), the total and the mean volumes (V_{tot} and V_{bar}) and the Weibull's shape factors *b* as calculated from Figure 10 (1.17 for the UVPs, 0.93 for the videography and not available for the water tank). The value of *Now* (not available for the water tank) differs of only 9 units (4-5%) among UVPs and videography, a deviation which is included in the measurement error of both the techniques. Similar considerations can be done for the values of V_{tot} and V_{bar}. In this case, the agreement among the videography and the traditional technique is even better, being the differences of 2 m^3/m (2%) and of $8\cdot10^{-5}$ m^3/m (2%) for V_{tot} and V_{bar} respectively.

Table 5. Number overtopping waves, total and mean volumes and Weibull's shape factors *b* resulting from the distribution of the individual overtopping volumes of the test TD4.

	Now	**V_{tot} [m^3/m]**	**V_{bar} [m^3/m]**	**Weibull's *b* factor**
Values from the water tank	-	0.85	4.50e-3	-
Values from the UVPs	194	0.79	4.03e-3	1.17
Values from the video-cluster analysis	183	0.83	4.58e-3	0.93

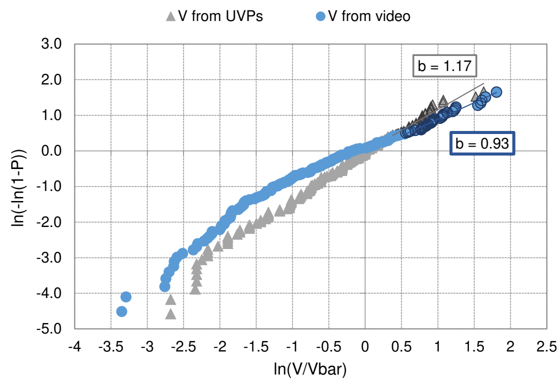

Figure 10. Probability distributions of the individual overtopping volumes of the test TD4 as reconstructed from the cluster analysis of the video of the experiments (blue circles) and from the UVPs (grey triangles). The *b*-values refer to the linear fitting of the upper 20% volumes.

5. Application of the methodology to the detection of the air entrainment

The detection of the flow areas subjected to turbulence and possible air entrainment would represent a key information for a number of applications, from the localization of the wave breaking, to the calibration of bi-phase numerical models (a.o., Gaeta and Lamberti, 2015), to the characterization of the wave impacts at walls, whose violence and intensity is directly connected to the aeration levels beneath the imping wave during the impact (a.o., Bullock et al., 2007).

As illustrated in Sub-section 3.4.2, the video-cluster analysis of the experiments was here applied to the estimation of the percentage of the flow areas characterized by air entrainment, in order to derive maps of the spatial and time map distribution of the bi-phase flow zones during the wave overtopping. The derivation of the space-time air entrainment maps is illustrated in the following, with reference to an example overtopping event and an example overtopping experiment. For sake of simplicity, this analysis is limited to the flow along the slope and the berm. The analysis of the flow before and over the wall and the study of the wave impact are objects of separate research.

The clustering of a frame provides a classification map of the flow, where each pixel composing the frame is labelled as “water”, “air entrainment” or other. Focusing on the air entrainment analysis, the labelling can be simplified to a “0-1” classification, where 1 is assigned to the pixels recognized as air entrainment and 0 otherwise. This information can be firstly processed to calculate the extent of the areas of air entrainment and localize their position in each frame.

The analysis of multiple air entrainment maps derived from consecutive frames can provide further qualitative and quantitative information about the concentration of the entrapped-air areas. Figure 11 shows an example of the time-stack evolution (12 frames, 0.4 s) of the air entrainment areas detected during an example overtopping event, from the generation of the first bi-phase flow zones around the berm off-shore edge (frame 1), to the collapse and breaking of the wave above the berm (frames 3 and 5), to the development into the bore flow (frames 7 and 9) and the dissipation of the last bi-phase flow areas just before the wall (frame 11). These images qualitatively show that the extent of the areas characterized by air entrainment tends to increase during the first part of the overtopping event, reaching a maximum at the wave breaking, while it starts decreasing during the bore flow. The images show also that before and during the wave breaking the air entrainment areas are relatively “compact” and their shape is influenced by the profile of the wave crest; on the contrary, after the wave breaking, the air entrainment areas are fragmented and tend to dissipate in many, small areas of irregular shape.

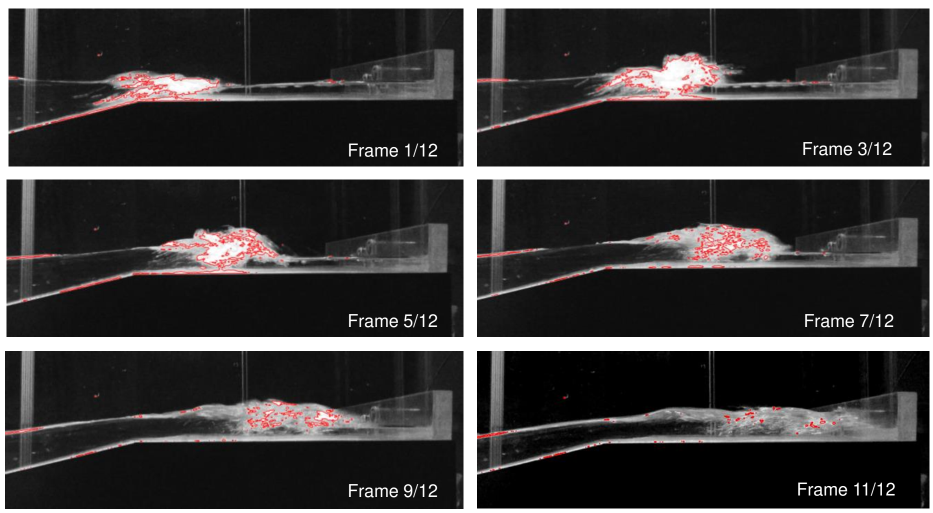

Figure 11. Time-evolution of an overtopping event and detection of the areas of air entrainment (red contour) through the video-cluster analysis.

The air entrainment map areas of the frames 1 to 6 and of the frames 7 to 12 composing the whole overtopping event portrayed in Figure 11 have been summed up, obtaining 2 “air entrainment sum maps”. The values of the pixels of such “sum maps” range between 0 and 6, in case the pixel is never or always affected by air entrainment, respectively. By normalizing the pixel values into the scale 0-1, it is possible to use the air entrainment sum maps to derive the spatial and time distribution of the air entrainment in the flow. Following this approach, the air entrainment concentration of each i-th pixel is defined as follows:

$$C_i = \frac{\text{pixel value from an air entrainment sum map}}{\text{maximum value of the air entrainment sum map}} \quad (9)$$

The 2 air entrainment sum maps relative to the frames 1 to 6 and 7 to 12 are represented in Figure 12, in normalized values and in comparison to the envelope of the free-surface derived for the corresponding 6 frames of each map. These maps provide a few quantitative information.

First, the extent and the concentration of the air entrainment is significantly higher during the frames 1 to 6 (Figure 12-top) than during the frames 7 to 12 (Figure 12-bottom), in agreement with the qualitative estimations given from Figure 11. This information is reported for each of the 12 frames in Table 6 in terms of ratio between the area of the flow affected by air entrainment and the total flow area (second column). Indeed, the air entrainment area represents the 17-28% of the total flow during the frames 1 to 6, while it is at maximum the 8.8% during the frames 7 to 12.

Second, Figure 12-top shows that the bi-phase flow is mostly localized close to the structure edge and in the middle of the overtopping tongue (yellowish colour), where the air entrainment concentration is equal to 1. On the contrary, in Figure 12-bottom the air entrainment concentration is more uniform and significantly lower, ranging between 0 and 0.4 at maximum (purple/magenta). The average values of air entrainment concentration calculated for each air entrainment sum map are reported in the columns 3 to 8 of Table 6. While during the frames 1 to 6 the highest C-values (1 or 0.83) represent the 5 and the 16% of the total air entrainment area, during the frames 7 to 12 the highest C-values are substantially null, and the lowest C-values (0.33 and 0.17) represent respectively the 29.8% and the 43.4% of the total air entrainment area.

Air entrainment sum maps similar to the example ones represented in Figure 12, relative to an overtopping event 12 frames-lasting, can be derived for the whole duration of the tests. In this case, the pixel-values of the sum maps may range between 0 and – ideally- the total number of frames of the test duration (typically, more than 16,000). However, the normalized concentration as defined in Eq. (9) still ranges between 0 and 1, and the same quantitative information derived for the example overtopping event can be derived for the whole test.

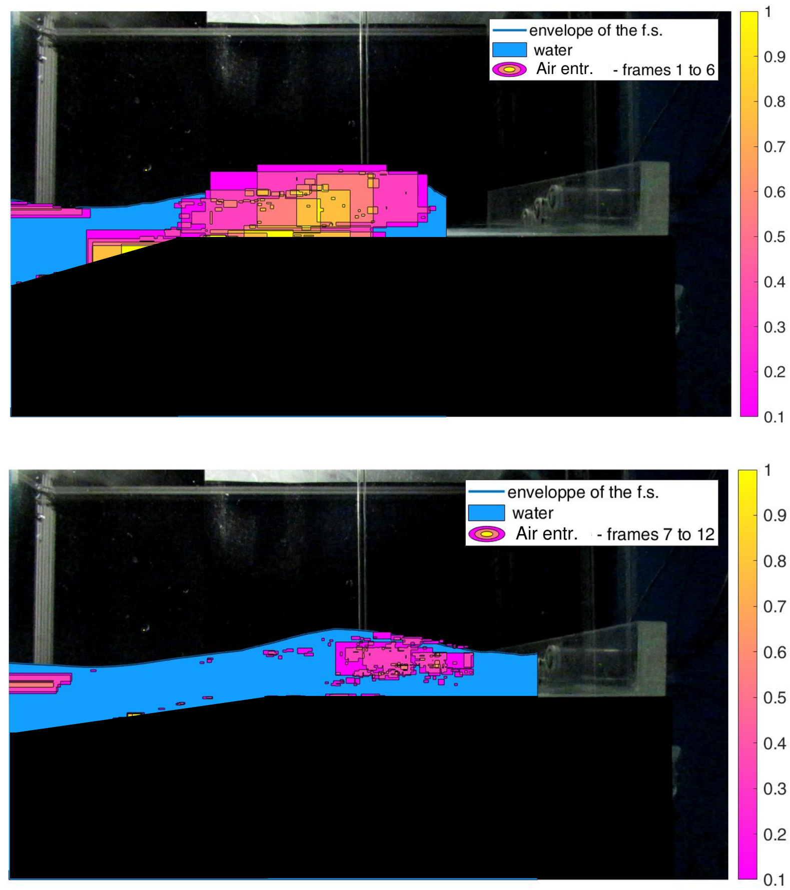

Figure 12. Air entrainment sum maps of the frames 1 to 6 (top) and 7 to 12 (bottom) of an overtopping event. The maps are compared to the envelope of the free-surface obtained over the corresponding 6 frames.

Table 6. Frame-by-frame percentage of the area of the flow subjected to air entrainment (first column) and concentration of the air entrainment over the frames 1 to 6 (first 6 rows) and over the frames 7 to 12 (last 7 rows) for an example overtopping event. Values derived from the air entrainment sum maps.

Frame	**(Air entr. area)/ (water area)**	Air entr. area with C=1 (6/6)	Air entr. area with C=0.83 (5/6)	Air entr. area with C=0.67 (4/6)	Air entr. area with C=0.5 (3/6)	Air entr. area with C=0.33 (2/6)	Air entr. area with C=0.17 (1/6)
1	27%	5.0%	16%	21%	17%	19%	22%
2	21%						
3	28%						
4	24%						
5	20%						
6	17%						
7	8.8%	0.48%	0.66%	6.7%	19.1%	29.8%	43.4%
8	7.2%						
9	4.3%						
10	1.4%						
11	1.0%						
12	0.8%						

6. Conclusions

This contribution presented the application of a video-cluster-based methodology to the modelling of the wave-structure interaction processes from the video recording of laboratory experiments of wave overtopping at sea-dikes with walls. The novelty of the contribution consists in the pre- and post-clustering procedures set up to improve the automatic detection of features from the images and in the direct and indirect outcomes of the application.

The pre-clustering techniques operate image subtraction, light and color adjustment and noise addition to optimize the pictures as taken from the camera for the automatic clustering phase. The post-clustering techniques handle the clustered maps as returned by the cluster analysis with morphological filters and iterative procedures to extract and elaborate the data embedded in the maps themselves.

The direct outputs of the whole videography methodology are the time series of the free-surface elevations along the dike slopes and berm and the spatial-time distribution of the areas of the flow affected by air entrainment. The derived outputs are the overtopping flow depths above the structure berm, the individual and total overtopping volumes and discharges and the time series of the flow celerities derived from the elaboration of the signals of the free-surface elevations "virtually" recorded through the video-analysis. These virtual quantities were derived for the first time from the results of a cluster analysis through the introduction of "virtual gauges" and the use of a procedure for the automatic detection and coupling of the individual overtopping events. The virtual quantities and compared to the corresponding quantities obtained from traditional measurements in the lab to verify and assess the accuracy of the methodology. The agreement among virtual and laboratory quantities is synthesized by the following relative errors: +36% for the extreme flow depths values ($h_{2\%}$); +19% and +25% for the average overtopping discharge estimated from the overtopping volumes and flow celerities, respectively; +5% for the estimation of the number of overtopping waves; +2% for the average and total overtopping volumes. The positive sign of the errors indicates that videography gave always conservative estimations of the virtual quantities. Such level of accuracy was achieved thanks to the introduction of the pre- and post-clustering techniques, whose ensemble represents a best practice to be recommended for other applications.

Another novel result of the research is represented by the maps of the concentration of the air entrainment related to the wave breaking and the turbulent overtopping flow. The eye-examination of these maps suggests that the areas of the flow more frequently subjected to the formation of air bubbles are accurately caught by the methodology. The time-stack values of the air entrainment concentration was reconstructed for an example overtopping event. This application allowed a detailed analysis of the spatial-time evolution of the concentration of air in the liquid phase. Specifically, it was found that the air entrainment is maximum around the berm off-shore edge and decreases radially towards the middle of the flow and the berm width (spatial distribution); it is maximum during the wave breaking, and starts decreasing during the bore flow (time-stack analysis). It should be noted that the air entertainment becomes 3D during the later stage of breaking since the flow is very turbulent. Therefore, the indications about the air entrainment mapping are valid for 2D conditions only and cannot be extended to a 3D domain, since just one camera was used to record the experiments.

List of notations

B	Berm width
c	Instantaneous wave celerity (front velocity of the overtopping tongue)
C	Air entrainment concentration
diswg	Distance between D1 and D3, corresponding approximately to the positions of the off-shore and in-shore edges of the berm, respectively
D1, D2, D3	Reference to the UVP 1, 2 and 3 installed along the berm
g	Acceleration due to gravity
h	Overtopping flow depths above the berm

$h_{2\%}$	Upper 2% percentile of the distribution of the *h*-values
h_b	Berm submergence (h_b<0 and h_b>0 respectively for emerged and submerged berm)
h_c	Elevation of the structure berm with respect to the bottom of the channel, excluding the crown wall
h_w	Height of the crown wall
H_{m0}	Spectral wave height
IE	Abbreviation of "in-shore edge"
K_r	Bulk wave reflection coefficient
$L_{m-1,0}$	Wave length from spectral analysis
Now	Number of overtopping waves
OE	Abbreviation of "off-shore edge"
q	Average specific wave overtopping discharge
q_{cel}	Value of q obtained from the integration of the overtopping wave celerities (c) with the overtopping flow depths (h)
q_{tank}	Value of q measured in the laboratory from the water tank
q_{Vol}	Value of q obtained from the sum of the V-values (V_{tot}) to the duration of the test (t_{tot})
swl	Acronym of "still water level"
R^2	Coefficient of determination
R_c	Structure freeboard with the respect to the still water level (R_c=h_w-h_b)
$s_{m-1,0}$	Wave steepness calculated based on the spectral wave period
t	Time
t_{tot}	Total duration of an experiment (corresponding to 480 s)
$T_{m-1,0}$	Spectral wave period
T_p	Peak wave periodo
u	Instantaneous flow velocity
UVP(s)	Acronym of "Ultrasonic Velocity Profilier(s)"

V	Instantaneous wave overtopping volume obtained from the integration of the *h*-values in the time domain
V_{bar}	Average wave overtopping volume of a test
V_{tot}	Total wave overtopping volume of a test
wgs	Acronym of "wave gauges"
α_d	Dike off-shore slope below the berm
γ_f	Structure roughness factor according to the EurOtop (2018) manual
μ	Mean
$\xi_{m-1,0}$	Iribarren-Battjes breaker parameter
$\sigma_{\%}$	Relative standard deviation (or coefficient of variation)

Author's contributions

Conceptualization, S.M.F and B.Z.; formal analysis, S.M.F., M.G.G. and M.G.; investigation, S.M.F., R.D.V. and M.G.G; data curation, S.M.F and R.D.V.; writing—original draft preparation, S.M.F.; writing—review and editing, M.G.G., M.G. and B.Z.; supervision, B.Z.

Acknowledgments

The support of the European Commission through the Horizon 2020 project BRIGAID ("BRIdging the GAp for Innovations in Disaster resilience," www.brigaid.eu) is gratefully acknowledged.

Data availability statement

The data that support the findings of this study are available from the corresponding author upon reasonable request.

References

Aleixo R., Soares-Frazão S. and Zech Y., 2018. Statistical analysis methods for transient flows–the dam-break case. J. Hydraul. Res.57, 688–701.

Almar R., Cienfuegos R., Catalán P.A., Michallet H., Castelle B., Bonneton P. and Marieu V., 2012. A new breaking wave height direct estimator from video imagery, Coastal Engineering 61, 42-48.

Almar, R., Blenkinsopp, C., Almeida, L.P., Cienfuegos, R., Catalán, P.A., 2017. Wave runup video motion detection using the radon transform. Coastal Engineering 130, 46–51. http://dx.doi.org/10.1016/j.coastaleng.2017.09.015.

Bechle, A.J., Wu, C.H., 2011. Virtual wave gauges based upon stereo imaging for measuring surface wave characteristics. Coastal Engineering 58 (4), 305–316. http://dx.doi.org/10.1016/j.coastaleng.2010.11.003.

Benetazzo A., Barbariol F., Bergamasco F., Torsello A., Carniel S., Sclavo, M., 2015. Observation of extreme sea waves in a space–time ensemble, J. Phys. Oceanogr. 45, 2261.

Blenkinsopp, C. E., and J. R. Chaplin (2007), Void fraction measurements in breaking waves, Proc. R. Soc. A, 463(2088), 3151–3170.

Blenkinsopp, C.E., Turner, I.L., Allis, M.J., Peirson, W.L., Garde, L.E., 2012. Application of LiDAR technology for measurement of time-varying free-surface profiles in laboratory wave flume. Coastal Engineering 68, 1–5.

Bouguet, J.Y. Camera Calibration Toolbox for Matlab. 2015. Available online: http://www.vision.caltech.edu/bouguetj/calib_doc/index.html (accessed on 1 September 2020).

Buscombe, D., Carini, R.J., Harrison, S.R., Chickadel, C.C., Warrick, J.A., 2020. Optical wave gauging using deep neural networks. Coastal Engineering 155, 103593. http://dx.doi.org/10.1016/j.coastaleng.2019.103593.

Buscombe, D., Carini, R.J., 2019. A Data-Driven Approach to Classifying Wave Breaking in Infrared Imagery, Remote Sensing 11, 859. http://dx.doi.org/10.3390/rs11070859.

Bullock, G.N., Obhrai, C., Peregrine, D.H. and Bredmose, H. (2007). Violent breaking wave impacts. Part 1: Results from large-scale regular wave tests on vertical and sloping walls, Coastal Engineering, 54, 602-617.

Canny, J., 1986. A computational approach to edge detection. IEEE Trans. Pattern Anal. Mach. Intell, 8, 679–714.

Carini, R.J., Chickadel, C.C., Jessup, A.T., Thomson, J., 2015. Estimating wave energy dissipation in the surf zone using thermal infrared imagery. J. Geophys. Res. Oceans 120, 3937–3957.

Chanson, H., 2002. Air–water flow measurements with intrusive phase-detection probes: Can we improve their interpretation, J. Hydraul. Eng., 128(3), 252–255.

Cox, D. T., and S. W. Shin (2003), Laboratory measurements of void fraction and turbulence in the bore region of surf zone waves, J. Eng. Mech., 129(10), 1197–1205

Deane, G. B. and Stokes, (2002), Scale dependence of bubble creation mechanisms in breaking waves, Nature, 418, 839–844.

Dempster, A. P., Laird, N. M. and Rubin, D. B., 1977. Maximum likelihood from incomplete data via the EM algorithm. Journal of the Royal Statistical Society. Series B (Methodological), 39(1), 1–38.

Den Bieman J.P., de Ridder M.P., van Gent M.R.A., 2020. Deep learning video analysis as measurement technique in physical models. Coastal Engineering 158, 103689.

De Vries, S., Hill, D.F., de Schipper, M.A., Stive, M.J.F., 2011. Remote sensing of surf zone waves using stereo imaging. Coastal Engineering 58 (3), 239–250. http://dx.doi.org/10.1016/j.coastaleng.2010.10.004.

Drazen, D. A., and W. K. Melville (2009), Turbulence and mixing in unsteady breaking surface waves, J. Fluid Mech., 628, 85–119.

Duin, R.P.W.; Pekalska, E., 2015. Pattern Recognition: Introduction and Terminology; Delft University of Technology: Delft, The Netherlands. Available online: http://resolver.tudelft.nl/uuid:f5c560ed-5fc7-4320-84b4-a20614012bc7 (last accessed July 1, 2021).

Duz, B., Scharnke, J., Hallmann, R., Tukker, J., Khurana, S. and K. Blanchard, 2020. Comparison of the CFD results to PIV measurements in kinematics of spilling and plunging breakers, Proceedings of the ASME 2020 39th International Conference on Ocean, Offshore and Arctic Engineering, OMAE2020-19268

EurOtop, 2018. Manual on wave overtopping of sea defences and related structures. An overtopping manual largely based on european research, but for worldwide application. N.W.H. Allsop, T. Bruce, J. DeRouck, A. Kortenhaus, T. Pullen, H. Schuttrumpf, P. Troch, J.W. van der Meer and B. Zanuttigh. www.overtoppingmanual.com.

Formentin, S.M., Zanuttigh, B., 2018. A new method to estimate the overtopping and overflow discharge at over-washed and breached dikes, Coastal Engineering 140, 240‑256.

Formentin S.M. and Zanuttigh B., 2019a. A Genetic Programming based formula for wave overtopping by crown walls and bullnoses, Coastal Engineering 152, 103529, 17 pp.

Formentin S.M. and Zanuttigh B., 2019b. Semi-automatic detection of the overtopping waves and reconstruction of the overtopping flow characteristics at coastal structures, Coastal Engineering 152, 103533, 18 pp.

Formentin S.M., Gaeta M.G., Palma G, Zanuttigh B., and Guerrero M., 2019a. Flow Depths and Velocities across a Smooth Dike Crest, Water 2019, 11, 2197; doi:10.3390/w11102197.

Formentin S.M., Zanuttigh B., Palma G, Gaeta M.G. and Guerrero M., 2019b. Experimental analysis of the wave loads on dike crown walls with parapets, Proc. of Coastal Structure Conference, Hannover (D), 2019.

Gaeta M.G., Guerrero M., Formentin S.M., Palma G. and Zanuttigh B., 2020. Non-Intrusive Measurements of Wave-Induced Flow over Dikes by Means of a Combined Ultrasound Doppler Velocimetry and Videography, Water 2020, 12, 3053; doi:10.3390/w12113053.

Gaeta, M.G., Lamberti, A., 2015. The role of air modeling on numerical investigation of coastal dynamics and wave-structure interactions, Computers & Fluids, 111, 114-126.

Hofland B., Diamantidou E., van Steeg P., Meys P., 2015. Wave runup and wave overtopping measurements using a laser scanner. Coastal Engineering 106, 20–29.

Hoque, A., and S. I. Aoki (2005), Distributions of void fraction under breaking waves in the surf zone, Ocean Eng., 32, 1829–1840

Holman, R. and J. Stanley, 2007. The history and technical capabilities of Argus. Coastal Engineering 54, 477-491.

Jessup, A., Zappa, C., Loewen, M., Hesany, V., 1997a, Infrared remote sensing of breaking waves. Nature 385, 52.

Jessup T., Zappa C.J., Yeh H., 1997b. Defining and quantifying microscale breaking waves with infrared imagery, J. Geophys. Res. 102, 23145.

Kimmoun, O. and H. Branger, 2007. A particle image velocimetry investigation on laboratory surf-zone breaking waves over a sloping beach, Journal of Fluid Mechanics, Vol.588, 353 – 397.

Li, H., Fernex, D., Semaan, R., Tan, J., Morzyński, M., & Noack, B., 2021. Cluster-based network model. Journal of Fluid Mechanics, 906, A21. doi:10.1017/jfm.2020.785

Lim, H. J., K. A. Chang, C. B. Su, and C. Y. Chen, 2008. Bubble velocity, diameter, and void fraction measurements in a multiphase flow using fiber optic reflectometer, Rev. Sci. Instrum., 79, 125105.

Lim, H.-J., K.-A. Chang, Z.-C. Huang, and B. Na (2015), Experimental study on plunging breaking waves in deep water, J. Geophys. Res. Oceans, 120, 2007–2049, doi:10.1002/2014JC010269

Mori, N., T. Suzuki, and S. Kakuno (2007), Experimental study of air bubbles and turbulence characteristics in the surf zone, J. Geophys. Res., 112, C05014, doi:10.1029/2006JC003647.

Mori, N., and S. Kakuno (2008), Aeration and bubble measurements of coastal breaking waves, Fluid Dyn. Res., 40, 616–626.

Na B., Chang K., Huang Z. and H. Lim, 2015. Turbulent flow field and air entrainment in laboratory plunging breaking waves, Journal of Geophysical Research: Oceans, 10.1002/2015JC011377,

Oh, S., Mizutani, N. and K. Suh, 2008. Laboratory observation of coherent structures beneath microscale and large-scale breaking waves under wind action, Experimental Thermal and Fluid Science, 32 (6), 1232-1247.

Perugini E., Soldini L., Palmsten M.L., Calantoni J. And Brocchini M., 2019. Linear depth inversion sensitivity to wave viewing angle using synthetic optical video, Coastal Engineering 152, 103535. https://doi.org/10.1016/j.coastaleng.2019.103535.

Raby A., Jayaratne R., Bredmose H. and Bullock G., 2028. Individual violent wave-overtopping events: Behaviour and estimation. J. Hydraul. Res. 58, 34-46.

Robinson I.S., Wells N.C., Charnock H., 1984. The sea surface thermal boundary layer and its relevance to the measurement of sea surface temperature by airborne and spaceborne radiometers, Int. J. Remote Sens. 5, 19.

Rojas, G., and M. R. Loewen (2010), Void fraction measurements beneath plunging and spilling breaking waves, J. Geophys. Res., 115, C08001, doi:10.1029/2009JC005614

Siddiqui M.H.K, Loewen M.R., Richardson C., Asher W.E., Jessup A., 2001. Simultaneous particle image velocimetry and infrared imagery of microscale breaking waves, Physics of Fluids 13, 1891. https://doi.org/10.1063/1.1375144

Streicher M., Hofland B., Lindenbergh R.C., 2013. Laser Ranging for Monitoring Water Waves in the new Deltares Delta Flume. ISPRS Annals of the Photogrammetry, Remote Sensing and Spatial Information Sciences, Volume II-5/W2, 2013.

Stringari, C.E., Harris, D.L., Power, H.E., 2019. A novel machine learning algorithm for tracking remotely sensed waves in the surf zone. Coastal Engineering 147, 149–158. http://dx.doi.org/10.1016/j.coastaleng.2019.02.002.

Stringari, C.E., Veras Guimarães P., Filipot J.F, Leckler F., Duarte R., 2021. Deep neural networks for active wave breaking classification, Scientific Reports 11:3604. https://doi.org/10.1038/s41598-021-83188-y

Techet, A.H. and A.K. McDonald, 2005. High Speed PIV of Breaking Waves on Both Sides of the AirWater Interface, 2005. Proc. 6th International Symposium on Particle Image Velocimetry, Pasadena, California, USA, September 21-23, 2005.

Vousdoukas M.I., Kirupakaramoorthy T., de la Torre M., Wübbold F., Wagner W., Schimmels S., Oumeraci H., 2014. The role of combined laser scanning and video techniques in monitoring wave-by-wave swash zone processes. Coastal Engineering 83, 150–165.

Wang, B. and Q. Liao, 2016. Field observations of turbulent dissipation rate profiles immediately below the air-water interface, Journal of Geophysical Research: Oceans, 4377-4391.

Waniewski, T. A., Brennen, C. E. and F. Raichlen, 2001. Measurements of Air Entrainment by Bow Waves, Journal of Fluids, 123, 57-63.

Zavadsky A., Benetazzo A., Shemer L., 2017. On the two-dimensional structure of short gravity waves in a wind wave tank, Physics of Fluids 29, 016601. https://doi.org/10.1063/1.4973319


PERICOLO
DI CADUTA


BOLOGNA

PLEASE CITE THIS ARTICLE AS DOI: 10.1063/5.0065019

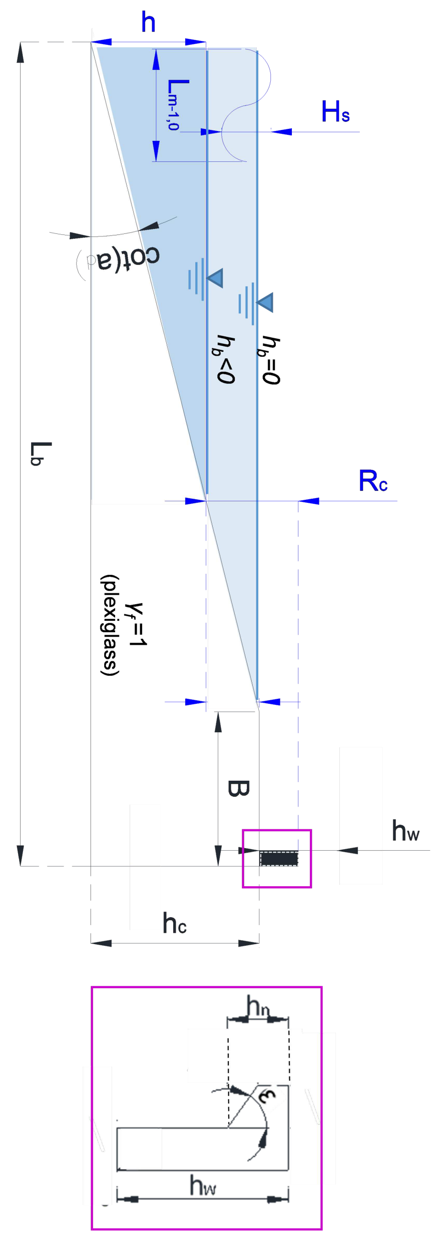

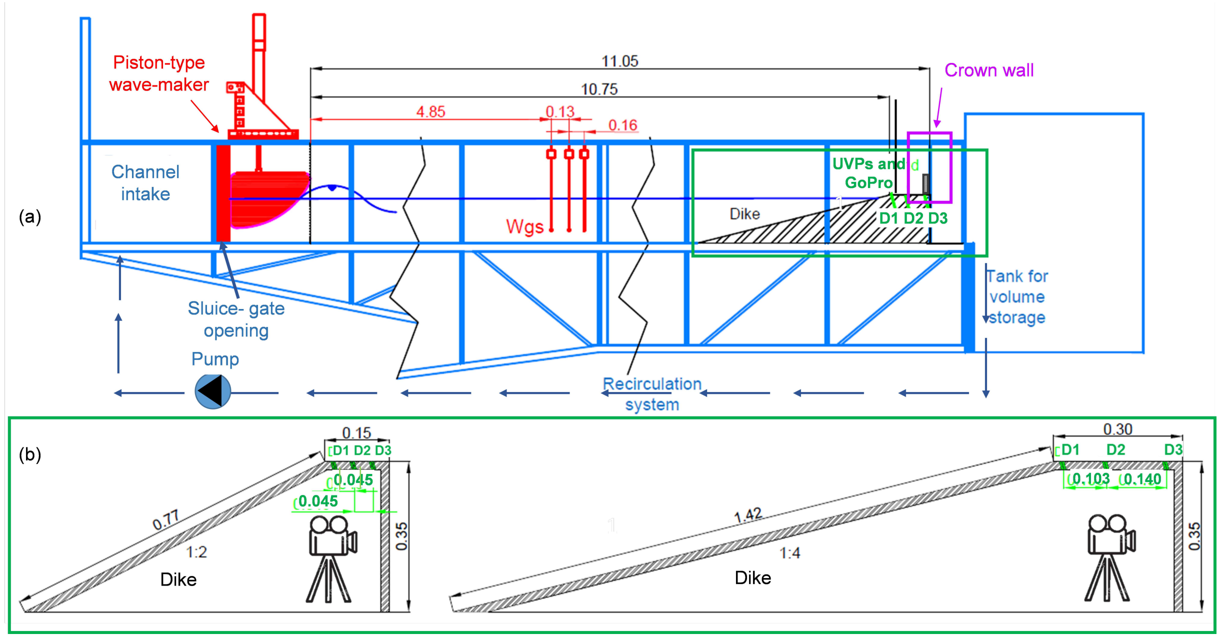
(a)
Piston-type
wave-maker
11.05
10.75
4.85
0.13
0.16
Crown wall
Channel
intake
Wgs
UVPs and
GoPro
Dike
D1 D2 D3
Sluice- gate
opening
Pump
Recirculation
system
Tank for
volume
storage
(b)
0.15
D1 D2 D3
0.045
0.045
0.77
1:2
Dike
0.35
0.30
D1
D2
D3
0.103
0.140
1.42
1:4
Dike
0.35

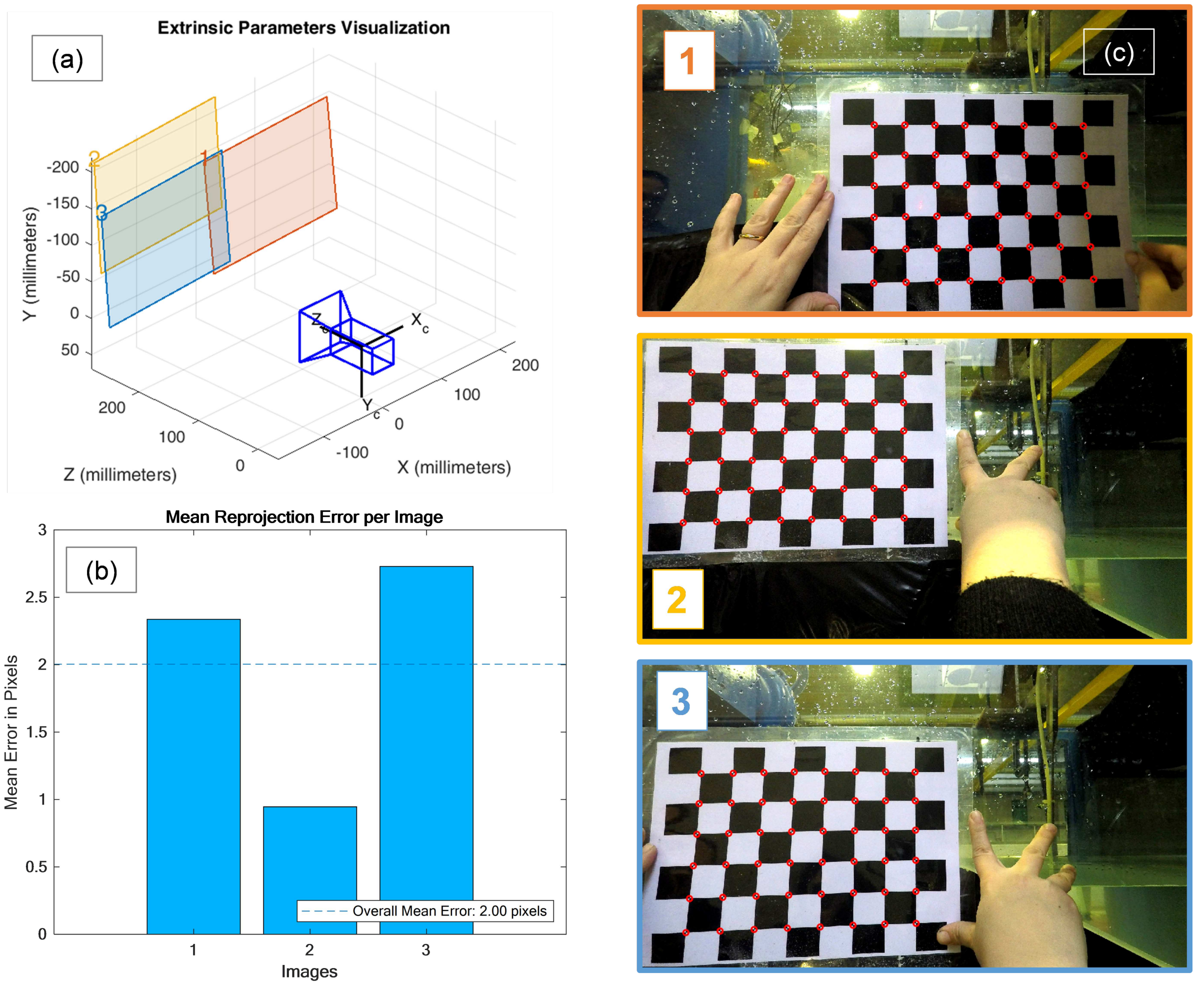
Extrinsic Parameters Visualization
(a)
Y (millimeters)
Z (millimeters)
X (millimeters)
Mean Reprojection Error per Image
(b)
Mean Error in Pixels
Images
Overall Mean Error: 2.00 pixels
(c)
1
2
3

PLEASE CITE THIS ARTICLE AS DOI: 10.1063/5.0065019

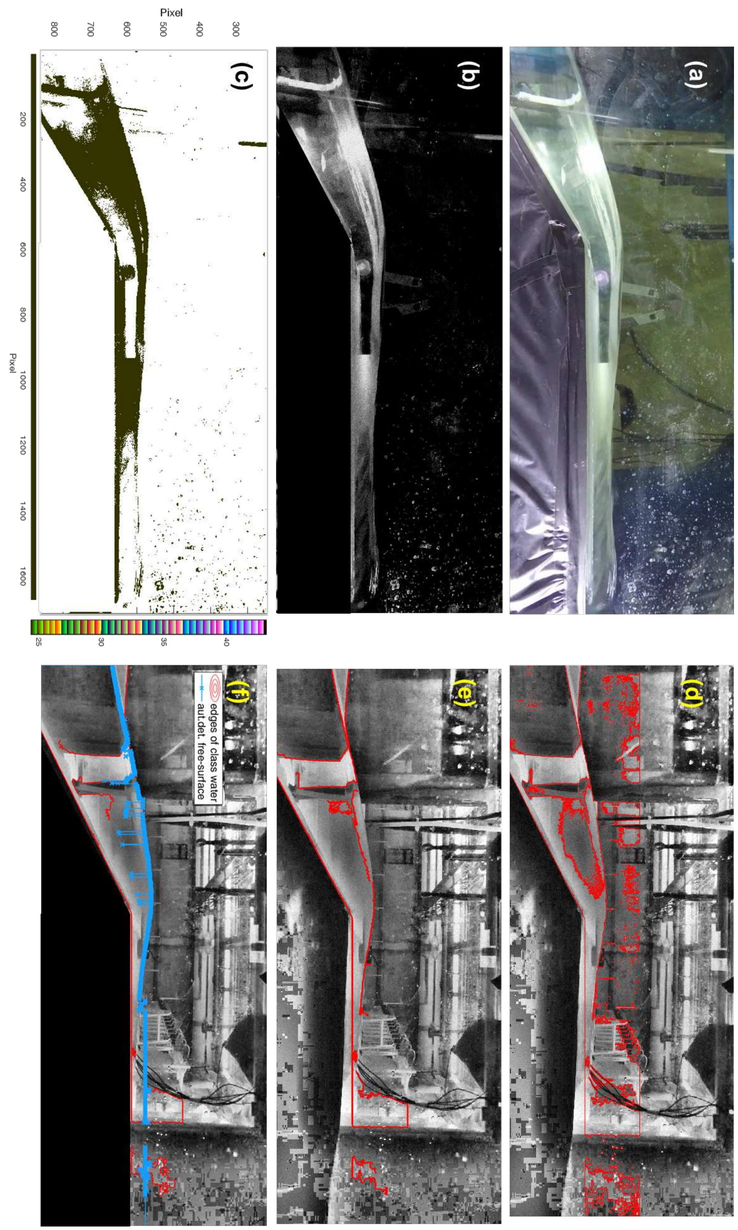

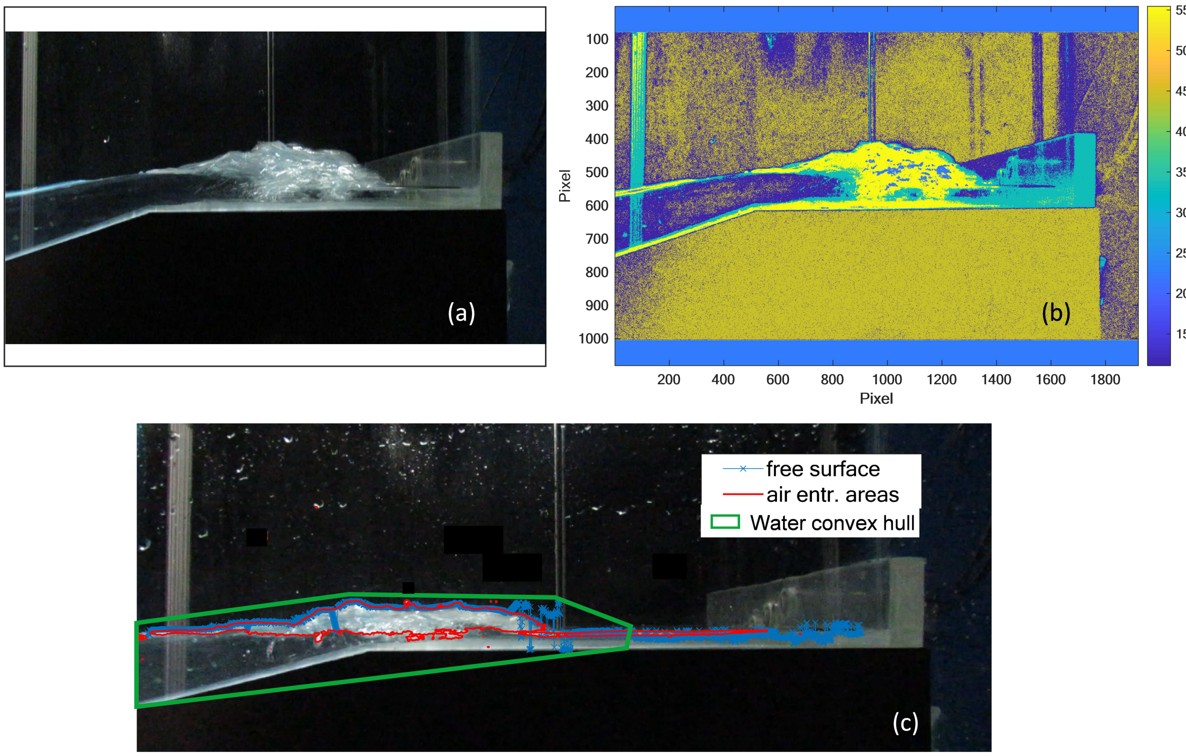
(a)
(b)
Pixel
Pixel
100
200
300
400
500
600
700
800
900
1000
200
400
600
800
1000
1200
1400
1600
1800
55
50
45
40
35
30
25
20
15
free surface
air entr. areas
Water convex hull
(c)

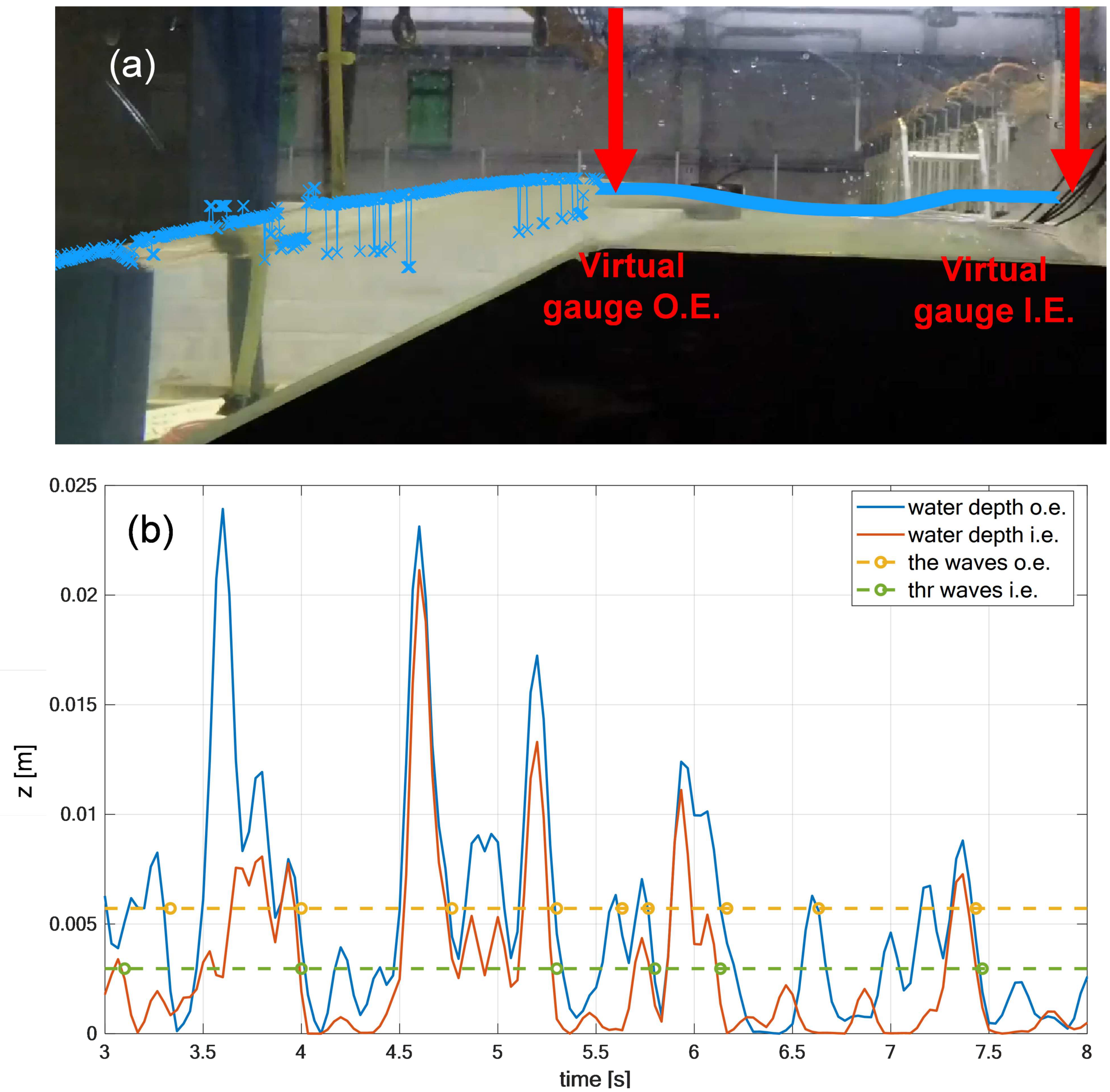
(a)
Virtual gauge O.E.
Virtual gauge I.E.
(b)
water depth o.e.
water depth i.e.
the waves o.e.
thr waves i.e.
z [m]
time [s]
0.025
0.02
0.015
0.01
0.005
0
3
3.5
4
4.5
5
5.5
6
6.5
7
7.5
8

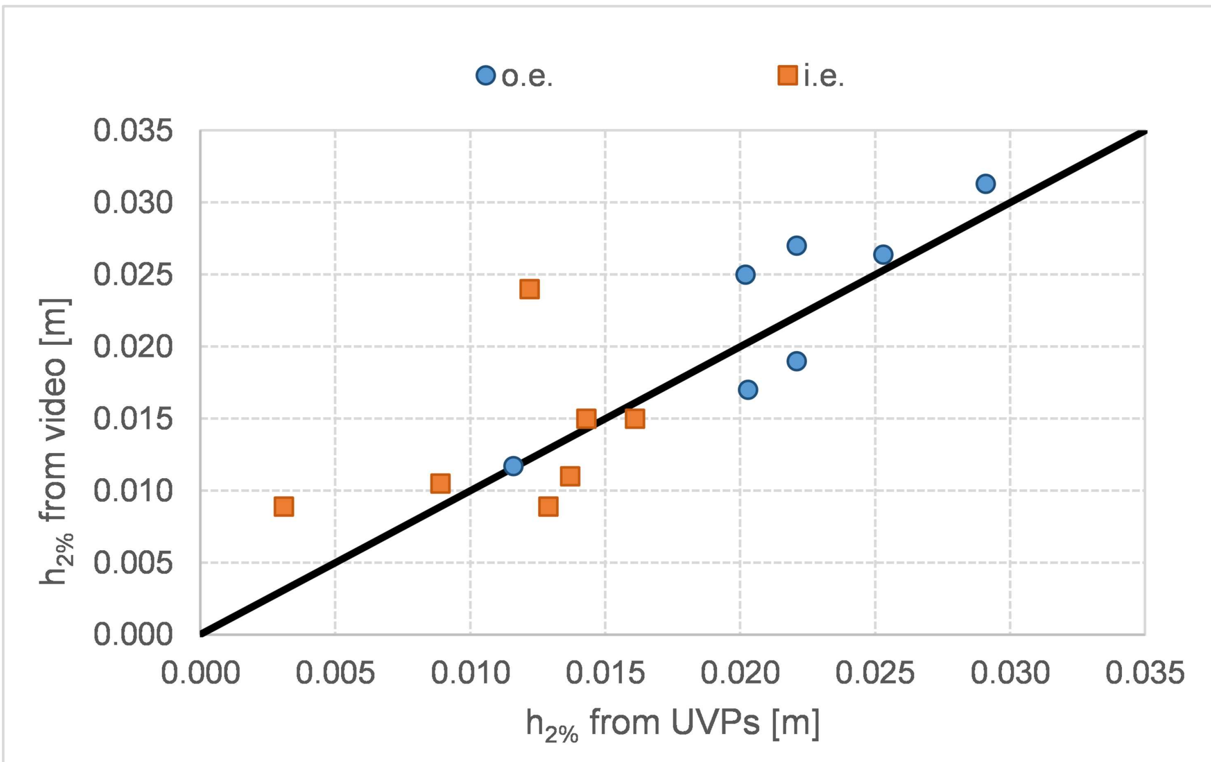
o.e.
i.e.
0.035
0.030
0.025
0.020
0.015
0.010
0.005
0.000
0.000
0.005
0.010
0.015
0.020
0.025
0.030
0.035
$h_{2\%}$ from video [m]
$h_{2\%}$ from UVPs [m]

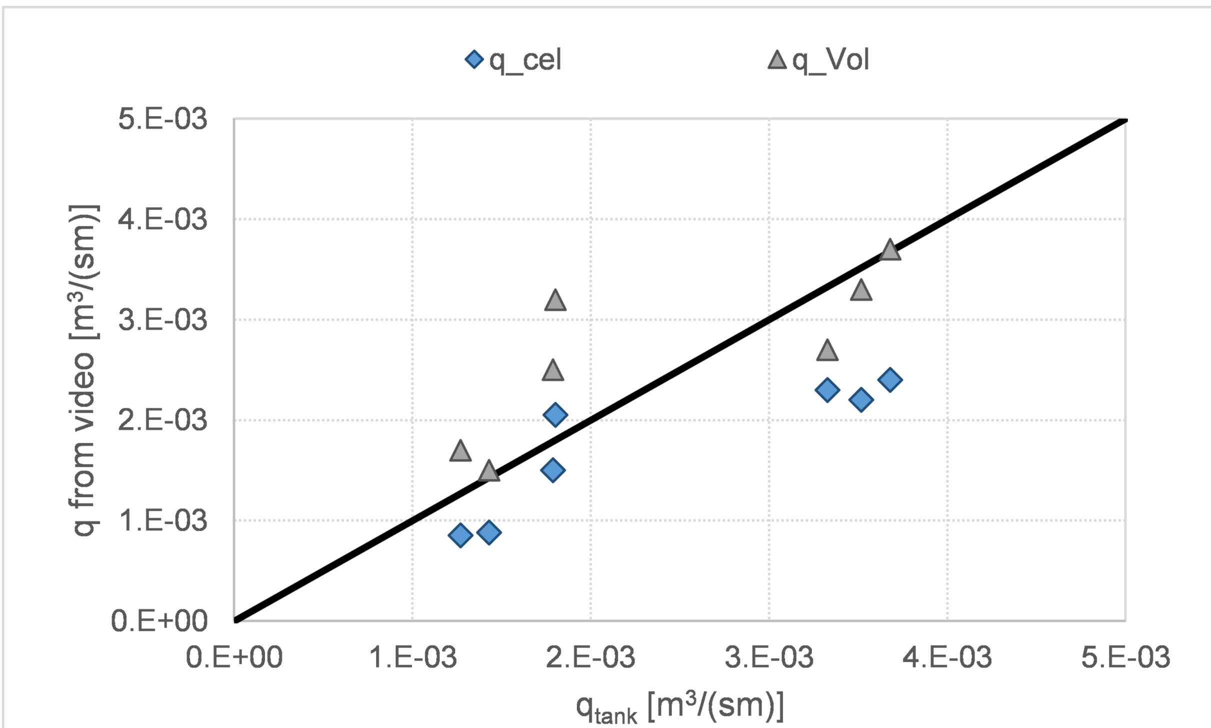
q_cel
q_Vol
q from video [m3/(sm)]
5.E-03
4.E-03
3.E-03
2.E-03
1.E-03
0.E+00
0.E+00
1.E-03
2.E-03
3.E-03
4.E-03
5.E-03
qtank [m3/(sm)]

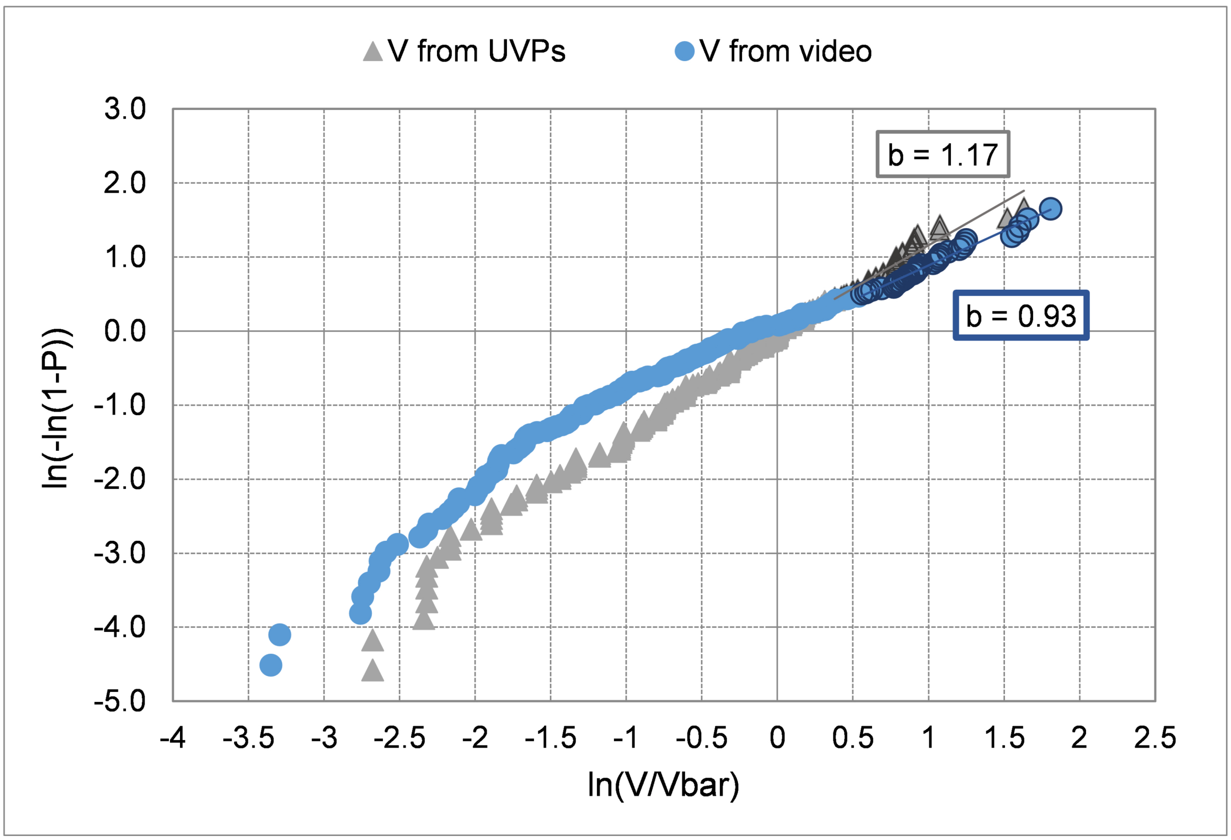
V from UVPs
V from video
b = 1.17
b = 0.93
3.0
2.0
1.0
0.0
-1.0
-2.0
-3.0
-4.0
-5.0
ln(-ln(1-P))
-4
-3.5
-3
-2.5
-2
-1.5
-1
-0.5
0
0.5
1
1.5
2
2.5
ln(V/Vbar)

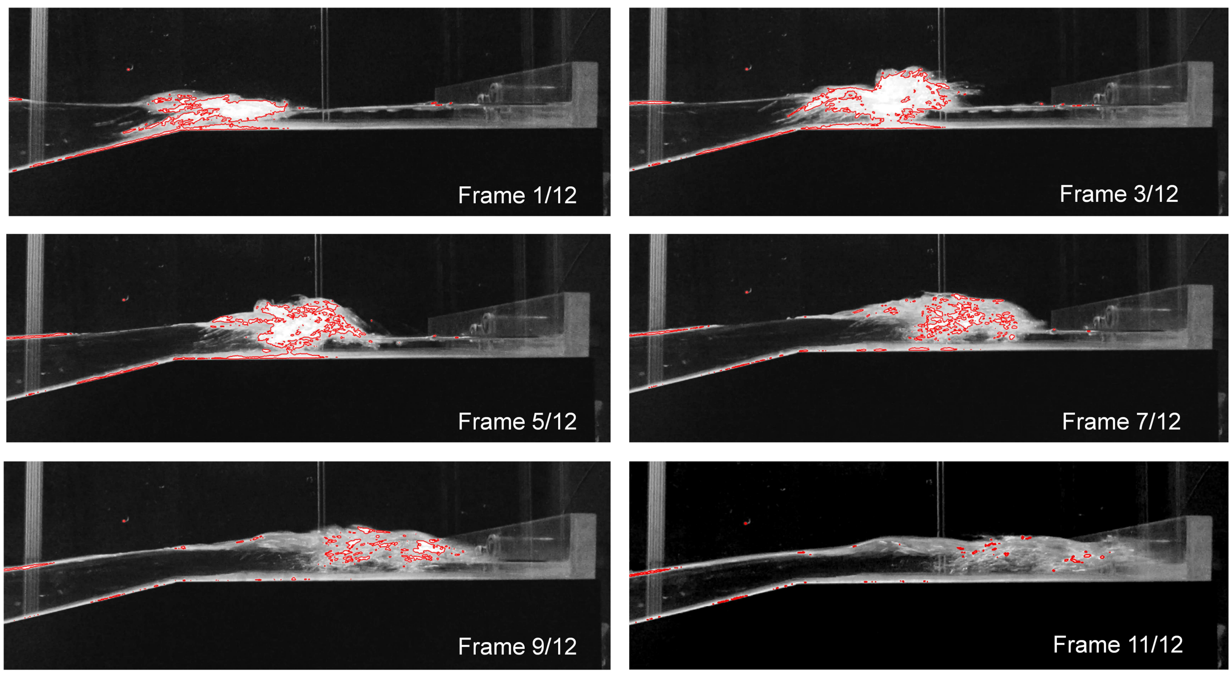
Frame 1/12
Frame 3/12
Frame 5/12
Frame 7/12
Frame 9/12
Frame 11/12

PLEASE CITE THIS ARTICLE AS DOI: 10.1063/5.0065019